JOURNAL OF PETROLOGY

Journal of Petrology, 2020, Vol. 61, No. 2: egaa018
doi: 10.1093/petrology/egaa018
Advance Access Publication Date: 17 February 2020
Original Article

OXFORD

Petrogenesis of the Ulungur Intrusive Complex, NW China, and Implications for Crustal Generation and Reworking in Accretionary Orogens

Gong-Jian Tang [1,2]*, Qiang Wang[1,2,3], Derek A. Wyman [4], Wei Dan[1,2], Lin Ma [1], Hai-Xiang Zhang[1] and Zhen-Hua Zhao[5]

[1]State Key Laboratory of Isotope Geochemistry, Guangzhou Institute of Geochemistry, Chinese Academy of Sciences, Guangzhou 510640, China; [2]CAS Center for Excellence in Tibetan Plateau Earth Science, Beijing 100101, China; [3]University of Chinese Academy of Sciences, Beijing 100049, China; [4]School of Geosciences, The University of Sydney, Sydney, New South Wales 2006, Australia; [5]Key Laboratory of Mineralogy and Metallogeny, Guangzhou Institute of Geochemistry, Chinese Academy of Sciences, Guangzhou 510640, China

*Corresponding author. Telephone: 86-20-85290297. Fax: 86-20-8529151. E-mail: tanggj@gig.ac.cn

Received March 5, 2019; Accepted February 7, 2020

ABSTRACT

Accretionary orogens are characterized by voluminous juvenile components (recently derived from the mantle) and knowing the origin(s) of such components is vital for understanding crustal generation. Here we present field and petrological observations, along with mineral chemistry, zircon U–Pb age and Hf–O isotope data, and whole rock geochemical and Sr–Nd isotopic data for the *c.*320 Ma Ulungur intrusive complex from the Central Asian Orogenic Belt. The complex consists of two different magmatic series: one is characterized by medium- to high-K calc-alkaline gabbro to monzogranite; the other is defined by peralkaline aegirine–arfvedsonite granitoids. The calc-alkaline and peralkaline series granitoids have similar depleted mantle-like Sr–Nd–Hf isotopic compositions, but they have different zircon $\delta^{18}O$ values: the calc-alkaline series have mantle-like $\delta^{18}O$ values with mean compositions ranging from $5{\cdot}2 \pm 0{\cdot}5‰$ to $6{\cdot}0 \pm 0{\cdot}9‰$ (2SD), and the peralkaline granitoids have low $\delta^{18}O$ values ranging from $3{\cdot}3 \pm 0{\cdot}5‰$ to $3{\cdot}9 \pm 0{\cdot}4‰$ (2SD). The calc-alkaline series were derived from a hydrous sub-arc mantle wedge, based on the isotope and geochemical compositions, under garnet peridotite facies conditions. This study suggests that the magmas underwent substantial differentiation, ranging from high pressure crystallization of ultramafic cumulates in the lower crust to lower pressure crystallization dominated by amphibole, plagioclase and minor biotite in the upper crust. The peralkaline series rocks are characterized by $\delta^{18}O$ values lower than the mantle and enrichment of high field strength elements (HFSEs) and heavy rare earth elements (HREEs). They likely originated from melting of preexisting hydrothermally altered residual oceanic crust in the lower crust of the Junggar intra-oceanic arc. Early crystallization of clinopyroxene and amphibole was inhibited owing to their low melting temperature, leading to HFSEs and HREEs enrichment in residual peralkaline melts during crystallization of a feldspar-dominated mineral assemblage. Thus, the calc-alkaline and peralkaline series represent episodes of crust generation and reworking, respectively, demonstrating that the juvenile isotopic signature in accretionary orogens can be derived from diverse source rocks. Our results show that reworking of residual oceanic crust also plays an important role in continental crust formation for accretionary orogens, which has not previously been widely recognized.

Key words: Central Asian Orogenic Belt; crust generation; crust reworking; granitoid; magmatic processes; mineral chemistry; zircon HF–O isotopes

INTRODUCTION

Accretionary orogens form along convergent plate margins and they are major sites of juvenile crust production (Cawood *et al.*, 2013 and references therein). They are characterized by the presence of voluminous juvenile components, as documented in the Arabian–Nubian Shield (Hargrove *et al.*, 2006), the Central Asian Orogenic Belt (CAOB) (Sengör *et al.*, 1993; Jahn *et al.*, 2000), the Tasmanides (Kemp *et al.*, 2009) and the Cordillera (Samson *et al.*, 1989). There is increasing evidence that continental crust generation takes place in different ways in different accretionary orogens, including outward growth of juvenile magmatic arcs, and mantle input during extensional, back-arc rifting episodes (Sengör *et al.*, 1993; Davidson & Arculus, 2006; Cawood *et al.*, 2009; Kemp *et al.*, 2009). However, juvenile arcs are built upon oceanic crust (Sengör *et al.*, 1993; Suzuki *et al.*, 2015) and probably consist largely of underthrust or trapped oceanic crust (Kay *et al.*, 1986; White *et al.*, 2003). It is difficult to distinguish magma sources of the juvenile components (i.e. sub-arc mantle wedge, subducted and residual oceanic crust, oceanic arc lower crust) in accretionary orogens because of their similar depleted radiogenic isotopic characteristics and the lack of distinctive isotopic criteria. Distinguishing these juvenile components is important for understanding crustal generation and reworking, and their roles in continental crust formation in accretionary orogens.

The CAOB is an outstanding natural laboratory for studying the origin of juvenile crustal components as it is considered to be the most important site of juvenile crustal growth in the Phanerozoic, as evidenced by the vast expanse of granitic and volcanic rocks with depleted Nd isotope compositions (Jahn, 2004). However, recent Nd–Hf isotopic data for felsic magmatic rocks have been used to argue that the volume of new crust has been grossly over estimated in the CAOB, which would not support models invoking unusually high crust generation rates during its accretionary history (Kröner *et al.*, 2014; 2017). Tang *et al.* (2017a) calculated the crustal generation rates from an analysis of Nd–Hf isotopic ratios in granitoid rocks from the Chinese Altai, Junggar and Tianshan segments of the CAOB, which formed at rates close to the overall global average for crust generation and involved only comparatively short periods of elevated magmatic activity. The issue is the extent to which the granitoids were generated via juvenile contributions from the mantle or by reworking of existing arc crustal sources, including residual oceanic crust. Therefore, continental crust formation, and the rates of crust generation and reworking, in these settings are not well understood.

This paper focuses on the Ulungur intrusive complex in the East Junggar, a portion of the CAOB. The Ulungur intrusive complex is characterized by various rocks including calk-alkaline and peralkaline series with depleted mantle-like Sr–Nd isotopic compositions that may be representative of magmatic rocks across the whole CAOB. Previous studies proposed that the Ulungur intrusive complex, including both the calc-alkaline and peralkaline series, is derived from a long-lived depleted mantle source (e.g. Han *et al.*, 1997), basaltic lower crust (e.g. Shen *et al.*, 2011) or remnants of oceanic crust in the lower crust (Liu *et al.*, 2013) based on their depleted mantle-like radiogenic isotopic compositions. In this study, we document a case where we have been able to overcome the difficulty associated with identifying juvenile sources for the CAOB (Fig. 1). We present new field and petrological observations, and new mineral chemistry, zircon U–Pb age and Hf–O isotope data, whole rock geochemical and Sr–Nd isotopic data. Our results provide new constraints on magma sources and crystallization processes of granitoids in the CAOB. They also distinguish juvenile components, which is important for understanding crustal generation and reworking and their respective roles in continental crust formation in accretionary orogens.

GEOLOGICAL BACKGROUND

Geological overview of the Junggar intra-oceanic arc

The CAOB is one of the largest accretionary orogenic belts in the world (Sengör *et al.*, 1993; Jahn, 2004; Kröner *et al.*, 2007; Windley *et al.*, 2007; Xiao *et al.*, 2015). It had a long and complex tectonic history from at least *c.*1·0 Ga, in the northern part of the orogen (Khain *et al.*, 2002), to *c.*250 Ma (Xiao *et al.*, 2003), and has been associated with the growth and consumption of the Paleo-Asian Ocean. It is characterized by accretion of a number of terranes including island arcs, ophiolites, accretionary prisms, and some microcontinents (Windley *et al.*, 2007).

The Junggar is located in the southwestern part of the CAOB (Fig. 1a), linking the Chinese Altai in the north with the Tianshan orogen in the south, and it is divided into eastern and western parts separated by the Junggar Basin (Xiao *et al.*, 2009) (Fig. 1b). It is a Paleozoic intra-oceanic island arc system with accretionary complexes, characterized by ophiolitic mélanges with volcanic rocks intruded by granitic plutons (Fig. 1b). Many ophiolitic mafic–ultramafic rocks occur in the Junggar region, and their ages range from the Cambrian to Early Carboniferous (*c.*500–370 Ma) (Tang *et al.*, 2007; Yang *et al.*, 2013; Ren *et al.*, 2014; Zhu *et al.*, 2015; Liu *et al.*, 2016; Luo *et al.*, 2017). The strata consist

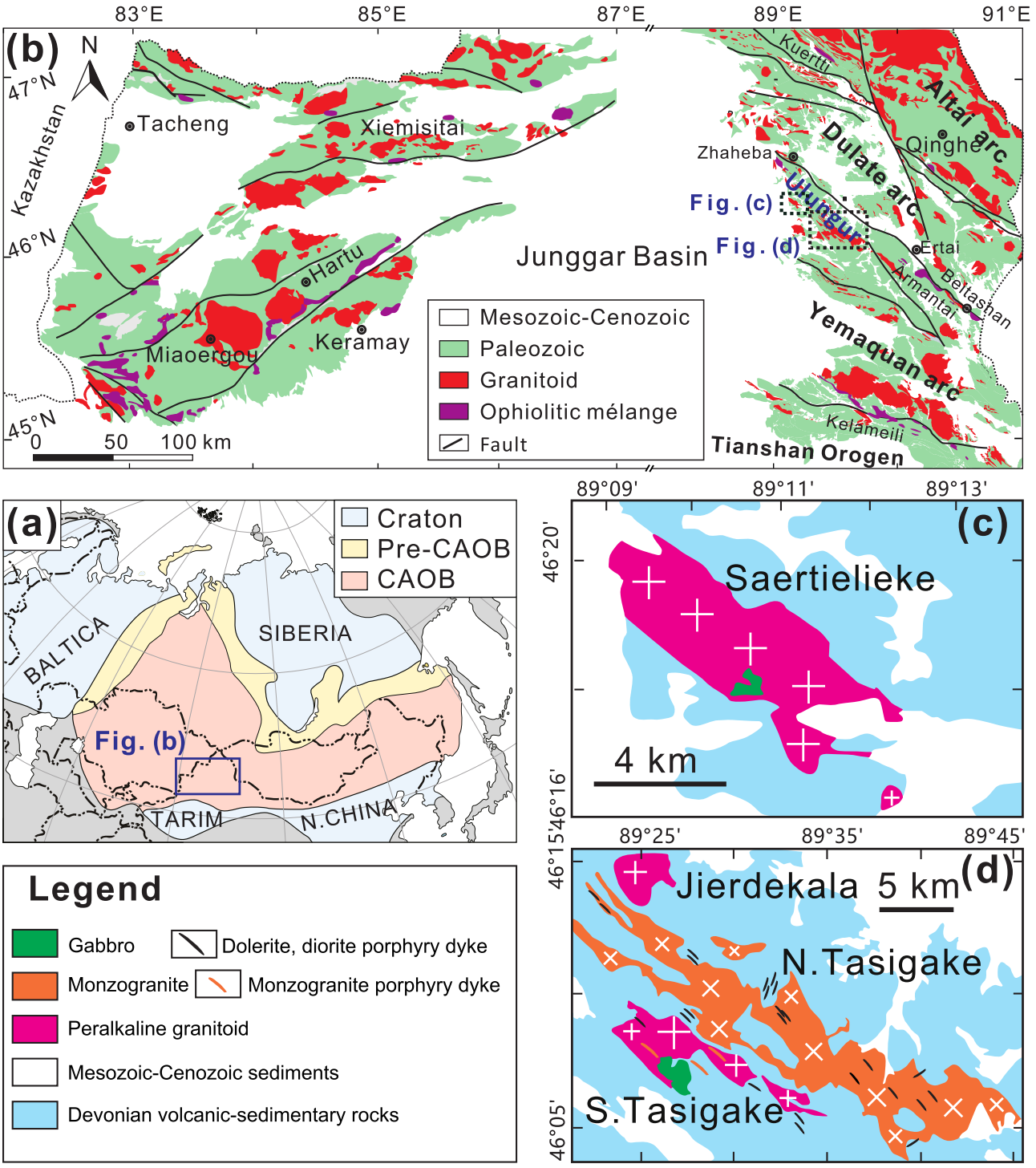

Fig. 1. (a) Simplified map of the Central Asian Orogenic Belt (CAOB) and surrounding cratons (after Jahn *et al.*, 2000). (b) Geological map of the Junggar, showing distribution of Paleozoic granitoids (Tang *et al.*, 2017a). (c–d) Outcrops of the Ulungur intrusive complex.

mainly of Devonian–Carboniferous and minor Silurian marine volcanic-sedimentary rocks (Zheng *et al.*, 2007; Zhang *et al.*, 2009; Geng *et al.*, 2011; Shen *et al.*, 2012; Liu & Liu, 2014; Shen *et al.*, 2014). Geochemical and isotopic evidence data indicate formation of the Junggar segment in an intra-oceanic arc setting (Chen & Jahn, 2004; Tang *et al.*, 2017*a*). The basement to the Junggar Basin largely consists of late Paleozoic volcanic rocks with minor shales and tuffs (Zheng *et al.*, 2007). No older basement has been documented in the Junggar region.

There are three NW–SE oriented ophiolite belts from north to south in East Junggar, the Kuerti, Zhaheba–Armantai and Kelameili, which extend eastward to

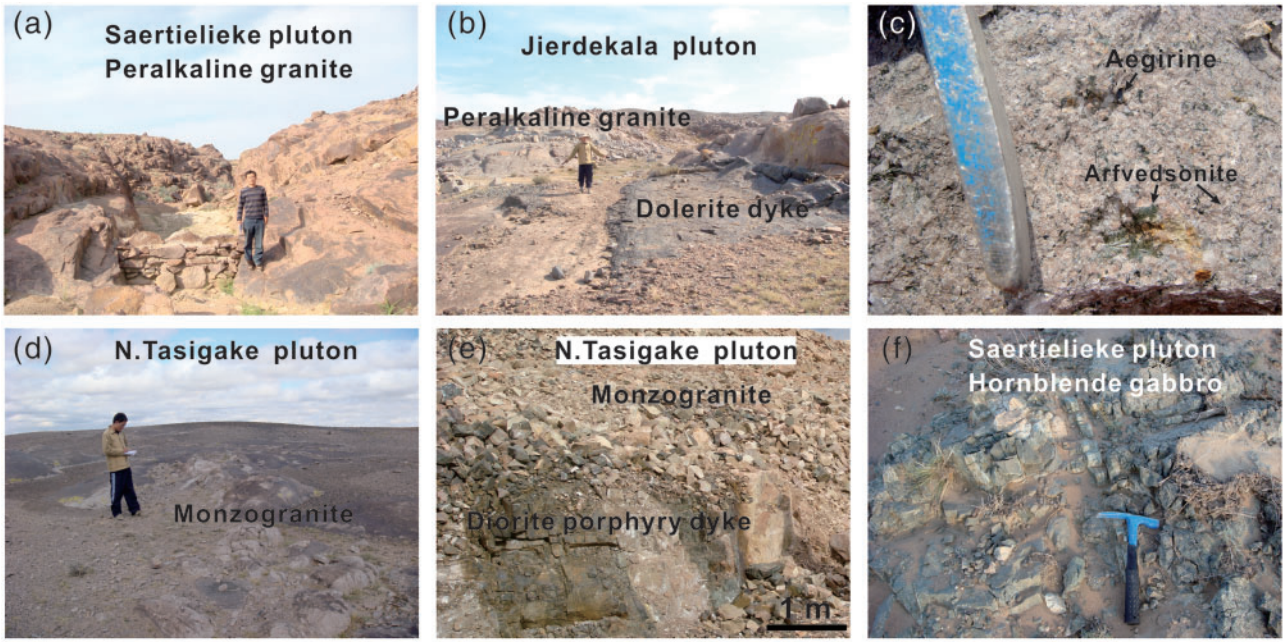

Fig. 2. Field photographs of the Ulungur intrusive complex. (a–b) Peralkaline granite plutons of Saertielieke and Jiedekala pluton, and some dolerite dykes intruded in to plutons. (c) Peralkaline granite of the Jiederkala pluton, which contains aegirine and arfvedsonite. (d–e) The North Tasigake pluton, and diorite porphyry dyke intruded in the pluton. (f) The gabbro of the Saertielieke pluton.

Mongolia. The Dulate arc in the north and Yemaquan arc in the south (Fig. 1b) are separated by the Zhaheba–Aermantai ophiolite belt (Xiao *et al.*, 2009; Zeng *et al.*, 2015; Liu *et al.*, 2016). Plagiogranites within the Zhaheba–Armantai ophiolite yielded zircon U–Pb dates of around 500 Ma (Xiao *et al.*, 2009; Zeng *et al.*, 2015; Liu *et al.*, 2016). Plagiogranites from the Kuerti and Kelameili ophiolites gave zircon U–Pb dates of around 390 Ma and 370 Ma, respectively (Tang *et al.*, 2007; Shen *et al.*, 2018).

The Junggar granitoid plutons

The most outstanding feature of the Junggar segment is the vast expanse of late Silurian–early Permian granitoid plutons and their volcanic equivalents, which occur throughout the segment (Chen & Arakawa, 2005; Zheng *et al.*, 2007; Geng *et al.*, 2009, 2011; Chen *et al.*, 2010; Shen *et al.*, 2011; Su *et al.*, 2012; Tang *et al.*, 2012*b*, 2017*a*; Liu *et al.*, 2013; Li *et al.*, 2014; Liu & Liu, 2014; Yin *et al.*, 2017) (Fig. 1b). U–Pb age dating of zircons from granitoid plutons within the Junggar segment indicates that most of them were emplaced during the late Carboniferous and early Permian, with a minority in the late Silurian and Early Carboniferous (Tang *et al.*, 2017*a*). The late Carboniferous and early Permian (*c.*320–280 Ma) granitoid plutons mainly occur in the Keramay area in West Junggar, and the Kelameili and Ulungur–Ertai areas in East Junggar. Some late Silurian and Early Carboniferous granitoid plutons are exposed in the Xiemisitai area in West Junggar, and the Zhaheba and Kouan areas in East Junggar.

Geochemically, these granitoid plutons consist of A-type and subordinate I-type granites, but the tourmaline-bearing muscovite granite dykes in the Eartaibei pluton from East Junggar display typical S-type characteristics (Tang *et al.*, 2017*b*). The A-type granites are dominantly composed of alkali-feldspar granite with minor arfvedsonite–aegirine granite. The I-type granites mainly consist of diorite, granodiorite and monzogranite (Fig. 1b).

Ulungur intrusive complex

The Ulungur intrusive complex is located *c.*15 km south of the Zhaheba–Armantai suture, in the NW corner of the Yemaquan arc (Fig. 1b). It consists of hornblende gabbro, monzogranite and peralkaline aegirine–arfvedsonite granite intruded into the Devonian strata, and NW–SE-trending dykes intruded into both the plutons and their volcanic host sequences (Fig. 1c,d). The Saertielieke, Jierdekala and South-Tasigake plutons consist of peralkaline granites, and the North-Tasigake pluton is composed of monzogranite. Two small hornblende gabbro intrusions occur within the Saertielieke and South-Tasigake plutons (Fig. 1c,d).

These plutons mainly have NW–SE elongated shapes (Fig. 1c,d). Previous studies indicate ages of about 325–291 Ma for the Ulungur intrusive complex (Shen *et al.*, 2011; Liu *et al.*, 2013). Both peralkaline granite and monzogranite plutons are cut by numerous NW–SE trending dykes, including both dolerite and diorite porphyry. In addition, a few peralkaline granite porphyry dykes have intruded into the Jierdekala pluton, and a few monzogranite porphyry dykes have intruded into the South Tasigake pluton. These dykes are variable in size but are mostly 0·5–1·5 m wide and less than 1 km long (Fig. 2).

Table 1: Petrographic summary

Lithology	SiO_2 (wt %)	Mg#	Mineral modes	Notes
Calc-alkaline series				
Hornblende gabbro	41·8–46·6	0·40–0·56	Pl (55–65%), Cpx (15–20%), Hb (10–20%), and trace Mag, Ti and Ap.	Medium-grained, orthocumulate texture. Pl and Cpx are euhedral. Some Cpx grains are replaced by Hb, and some Hb occur as poikilitic.
Dolerite dyke	50·1–53·0	0·42–0·52	Pl (70–80%), Cpx (15–25%), Hb (2–5%), and trace Mag, Ti and Ap.	Medium- to fine-grained (0·5–1·5 mm) ophitic texture. Pl is euhedral, and Cpx is subhedral or anhedral. Some Cpx grains occur as inclusions in Pl.
Diorite porphyry dyke	57·9–64·9	0·40–0·49	Pl (60–70%), Cpx (10–20%), Qtz (10–15%), Bi (<5%), Hb (<5%), K-spar (<5%), and trace Mag, Ti, Ap and Zr.	Fine- to medium-grained, porphyritic texture. Pl and Cpx are subhedral or anhedral. Qtz, Bi, Hb and K-spar are anhedral. Some Pl grains occur as inclusions in Cpx.
Monzogranite	69·1–76·4	0·25–0·39	Pl (30–40%), K-spar (35–40%), Qtz (20–25%), Hb (2–5%), Bi (1–2%), and trace Mag, Ti, Ap and Zr.	Medium-grained porphyritic or equigranular texture.
Peralkaline series				
Syenitic granite	67·6–39·4	0·21–0·29	K-spar (65–70%), Pl (10–15%), Qtz (10–15%), Arf (2–5%), Aeg (1–2%), and trace Mag, Ap and Zr.	Fine-grained porphyritic texture. Arf and Aeg occurs as subhedral or anhedral.
Peralkaline granite	73·6–77·4	0·02–0·17	K-spar (60–70%), Qtz (25–35%), Pl (0–3%), Arf (2–5%), Aeg (2–5%), and trace Mag, Ap, Zr and perovskite.	Medium to fine grained or porphyritic texture. The peralkaline granite porphyry dykes show porphyritic texture, and mafic minerals make up 5% of them and arechiefly arf. Aeg occurs as phenocrysts in most peralkaline granites, and also occurs in the later crystallization sequence where it replaces arf. Arf occurs as subhedral or anhedral.

Cpx, clinopyroxene, Pl, plagioclase; K-spar, K-feldspar; Hbl, hornblende; Bt, biotite; Qz, quartz; Aeg, aegirine; Arf, arfvedsonite; Hb, hornblende; Zr, zircon; Ap, apatite; Mag, magnetite; Ti, ilmenite.

FIELD OBSERVATIONS AND PETROGRAPHY

Petrographic descriptions are summarized in Table 1. Hornblende gabbros, from the Saertielieke and South-Tasigake plutons, are almost exclusively composed of large clinopyroxene and plagioclase crystals (Fig. 3a), although Fe–Ti oxides are abundant. Some clinopyroxenes are replaced by hornblende along rims, cracks and cleavage planes (Fig. 3b). Some samples are characterized by a high proportion of poikilitic hornblende that includes clinopyroxene, plagioclase and Fe–Ti oxides (Fig. 3c). The dolerite dykes show a medium- to fine-grained (0·5–1·5 mm) ophitic texture. The major minerals are plagioclase and clinopyroxene with minor hornblende (Fig. 3d). The diorite porphyry dykes consist of plagioclase, alkali feldspar, hornblende, biotite and quartz (Fig. 3f). The monzogranites display a medium-grained porphyritic or equigranular texture, and consist of plagioclase, alkali feldspar, quartz, with minor hornblende and biotite (Fig. 3g,h). Plagioclase occurs as blocky, euhedral tablets that are oscillatory-normal zoned. Dark-brown biotite is euhedral to subhedral. Euhedral to subhedral hornblende is typically prismatic. Some hornblende grains are green and poikilitic (Fig. 3g).

The peralkaline granites show medium to fine grained texture and are mineralogically similar among the different plutons (Fig. 3h,l). These rocks are composed mainly of quartz, perthite, aegirine, arfvedsonite and minor accessory minerals (e.g. zircon, apatite, magnetite and perovskite). Aegirine and arfvedsonite are ubiquitous phases and are the dominant primary mafic minerals in all samples. Aegirine occurs as phenocrysts in most peralkaline granites, but also occurs in the later crystallization sequence where it replaces arfvedsonite along fractures, cleavages, and around rims. The phenocrysts are euhedral with a grass greenish pleochroism, occurring with a contemporaneous magmatic assemblage of quartz, perthite, apatite and zircon. Arfvedsonite varies from brown or dark blue to nearly opaque in thin section and occurs either as euhedral or subhedral crystals adjacent to quartz and perthite.

ANALYTICAL METHODS

Mineral composition analyses

Major element analysis and backscattered electron (BSE) imaging of minerals were carried out using a JEOL JXA-8230 electron microprobe Superprobe at the College of Earth Sciences, Guilin University of Technology. An accelerating voltage of 15 kV, a specimen current of $3{\cdot}0 \times 10^{-8}$ A, and a beam size of 1–2 μm were employed. The data reduction was carried out using ZAF correction.

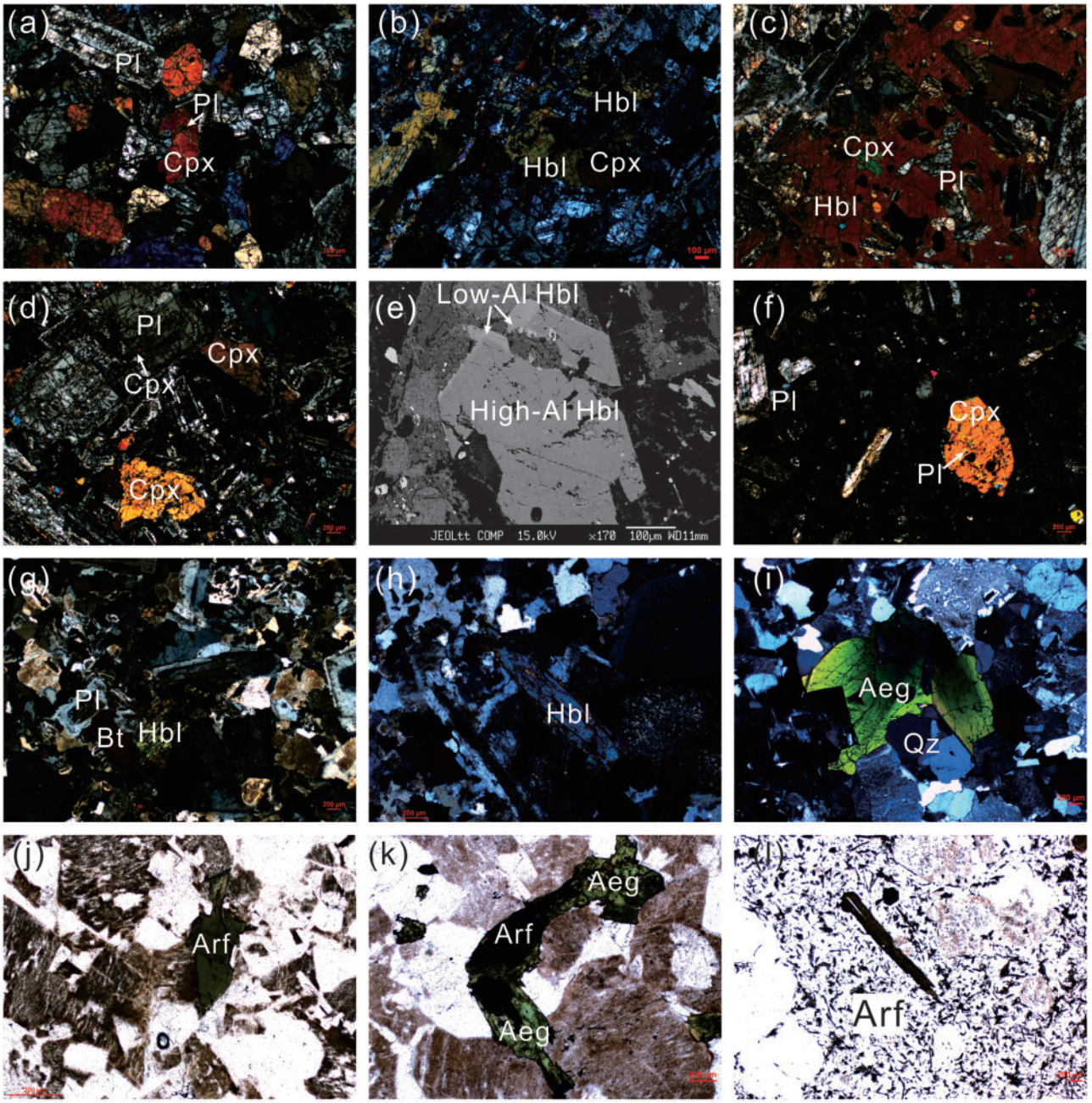

Fig. 3. Photomicrographs of samples from the Ulungur intrusive complex. (a–c) gabbro, which is mainly composed of clinopyroxene and plagioclase. Some clinopyroxenes are replaced by hornblende. Some samples are characterized by a high proportion of poikilitic hornblende (c). (d–e) Dolerite dyke; some amphibole crystals show an abrupt shift in Al_2O_3 content at the core-rim boundary. (f) Diorite porphyry dykes. (g–h) Monzogranite, which consists of plagioclase, alkali feldspar and quartz, with minor hornblende and biotite. (i–l) Peralkaline granitoids, which are composed mainly of quartz, perthite, aegirine and arfvedsonite. Aegirine replaces arfvedsonite in the later crystallization sequence (k). Cpx, clinopyroxene; Pl, plagioclase; Hbl, hornblende; Bt, biotite; Qz, quartz; Aeg, aegirine; Arf, arfvedsonite.

In situ trace elements were measured with an ELEMENT XR (Thermo Fisher Scientific) ICP-MS coupled with a 193-nm (ArF) Resonetics RESOlution M-50 laser ablation system in the State Key Laboratory of Isotope Geochemistry, Guangzhou Institute of Geochemistry, Chinese Academy of Sciences (GIG-CAS). Laser operating conditions were set as follows: beam size, 33 μm; repetition rate, 6 Hz; energy density, *c.*4 J cm^{-2}. A smoothing device (The Squid, Laurin Technic) was used to smooth the sample signal. Each spot analysis consisted of 20 s gas blank collection with the laser off, and 30 s sample signal detection with the laser on. Measurement was conducted under the E scan mode (scanning the electric field). Signals of the following masses were detected: ^{25}Mg, ^{29}Si, ^{43}Ca, ^{45}Sc, ^{47}Ti, ^{51}V, ^{53}Cr, ^{55}Mn, ^{57}Fe, ^{59}Co, ^{63}Cu, ^{66}Zn, ^{71}Ga, ^{85}Rb, ^{88}Sr, ^{89}Y, ^{90}Zr, ^{93}Nb, ^{137}Ba, ^{139}La, ^{140}Ce, ^{141}Pr , ^{146}Nd, ^{147}Sm, ^{151}Eu, ^{157}Gd, ^{159}Tb, ^{162}Dy, ^{165}Ho, ^{166}Er, ^{169}Tm, ^{174}Yb,

^{175}Lu, ^{178}Hf, ^{181}Ta, ^{208}Pb, ^{232}Th and ^{238}U. Si, pre-measured with EPMA, was selected as the internal standard element. The calibration line for each element was constructed by analysing three USGS reference glasses BCR-2G, BHVO-2G and GSD-1G. The oxide molecular yield, indicated by the $^{238}U^{16}O/^{238}U$ ratio, was less than 0·3%. The detailed experimental procedure and data reduction strategy are described in Zhang *et al.* (2019). A USGS reference glass TB-1G was repeatedly measured as an unknown sample. Thirty analyses of TB-1G indicate most elements are within 8% of the reference values and the analytical precision (2RSD) was better than 10% for most elements.

Zircon cathodoluminescence

Cathodoluminescence (CL) images of zircons were obtained using a Carl Zeiss Field Emission Scanning Electron Microscope (FESEM) + Gatan MonnCL4 at GIG-CAS, in order to characterize internal structures and choose potential target sites for U–Pb dating and Hf–O isotope analysis.

SIMS zircon U–Pb and O isotope methods

Zircon oxygen isotopes were measured using the Cameca IMS-1280 SIMS at GIG-CAS. The detailed analytical procedures were the same as those described by Li *et al.* (2010*b*). The measured oxygen isotopic data were corrected for instrumental mass fractionation (IMF) using the Penglai zircon standard (δ^{18}OVSMOW = 5·3‰) (Li *et al.*, 2010*b*). The internal precision of a single analysis generally was better than 0·2‰ (1σ standard error) for the $^{18}O/^{16}O$ ratio. The external precision, measured by the reproducibility of repeated analyses of Penglai standard, was 0·41‰ (2SD, n = 120). Ten measurements of the Qinghu zircon standard during the course of this study yielded a weighted mean of $\delta^{18}O = 5·3 \pm 0·6$‰ (2SD), which is consistent within errors with the reported value of 5·3 ± 0·3‰ (Li *et al.*, 2010*b*; 2013). Measurements of U, Th and Pb for most samples were conducted using the Cameca IMS-1280 HR SIMS at GIG-CAS. The analytical procedures were the same as those described by (Li *et al.*, 2009). A long-term uncertainty of 1·5% (1σ RSD) for $^{206}Pb/^{238}U$ measurements of standard zircons was propagated to the unknowns (Li *et al.*, 2010*a*), despite the fact that a few individual $^{206}Pb/^{238}U$ measured errors during the course of this study were 1% (1σ RSD) or less. The ellipsoidal spot is about 20 × 30 μm in size. U–Th–Pb ratios were determined relative to the *c.*337 Ma standard zircon Plešovice (Sláma *et al.*, 2008). Uncertainties on individual analyses in the data tables are reported at a 1σ level. Mean ages for pooled U/Pb analyses are quoted with 2σ and/or 95% confidence intervals.

LA-ICPMS zircon U–Pb dating method

U–Pb isotope compositions of zircon grains from three samples were analysed with an Agilent Q-ICPMS connected to a 193 nm excimer laser ablation system at the Institute of Geology and Geophysics, Chinese Academy of Sciences in Beijing, China (IGG-CAS). The GeoLas PLUS 193 nm excimer ArF laser ablation system is the upgrade product of GeoLas CQ made by Lambda Physik in Germany. Helium carrier gas transported the ablated sample materials from the laser-ablation cell via a mixing chamber to the ICPMS after mixing with Ar gas. Zircon 91500 was used as the standard and the standard silicate glass NIST 610 was used to optimize the machine, with a beam diameter of 30 μm Raw count rates for ^{29}Si, ^{204}Pb, ^{206}Pb, ^{207}Pb, ^{208}Pb, ^{232}Th and ^{238}U were collected and U, Th and Pb concentrations were calibrated using ^{29}Si as the internal calibrant and NIST 610 as the reference material. $^{207}Pb/^{206}Pb$ and $^{206}Pb/^{238}U$ ratios were calculated using the GLITTER program (Jackson *et al.*, 2004). Measured $^{207}Pb/^{206}Pb$, $^{206}Pb/^{238}U$ and $^{208}Pb/^{232}Th$ ratios in zircon 91500 were averaged over the course of the analytical session and used to calculate correction factors. These correction factors were then applied to each sample to correct for both instrumental mass bias and depth-dependent elemental and isotopic fractionation. The age calculations were made using Isoplot (ver. 3·00) (Ludwig, 2003).

LA-MC-ICPMS zircon Hf isotope method

Subsequently, in situ zircon Hf isotopic analyses were conducted using a Neptune MC–ICPMS, equipped with a 193-nm laser, at IGG-CAS. During analyses, spot sizes of 32 and 63 mu, with a laser repetition rate of 10 Hz at 100 mJ, were used and raw count rates for ^{172}Yb, ^{173}Yb, ^{175}Lu, mass 176 (Hf + Yb + Lu), ^{177}Hf, ^{178}Hf, ^{179}Hf, ^{180}Hf and ^{182}W were collected. During laser ablation analyses, the isobaric interference of ^{176}Lu on ^{176}Hf is negligible due to the extremely low $^{176}Lu/^{177}Hf$ in zircon (normally < 0·002). However, interference of ^{176}Yb on ^{176}Hf must be carefully corrected since the contribution of ^{176}Yb to ^{176}Hf may profoundly affect the accuracy of the measured $^{176}Hf/^{177}Hf$ ratio. In this study, the mean $^{173}Yb/^{171}Yb$ ratio of the individual spots was used to calculate the fractionation coefficient (βYb) and then to calculate the contribution of ^{176}Yb to ^{176}Hf. During analysis, an isotopic ratio of $^{176}Yb/^{172}Yb = 0·5887$ was applied. The detailed analytical technique is described in Wu *et al.* (2006). During the analytical period, the $^{176}Hf/^{177}Hf$ and $^{176}Lu/^{177}Hf$ ratios of the standard zircon (91500) were 0·282294 ± 15 ($2\sigma_n$, n = 20) and 0·00031, similar to the low peaks of $^{176}Hf/^{177}Hf$ ratios of 0·282284 ± 22 measured by (Griffin *et al.*, 2006), also using the laser method.

Whole-rock geochemistry and Sr–Nd isotopic analyses

Whole rock major element oxides were determined by standard X-ray fluorescence (XRF) methods as described by Li *et al.* (2006). Trace elements were analysed by inductively coupled plasma mass spectrometry (ICP-MS), using a Perkin-Elmer Sciex ELAN 6000

instrument at the GIG-CAS. Analytical precisions for most elements are better than 5%.

Sr and Nd isotopic analyses were performed on a Micromass Isoprobe multicollector ICP-MS at the GIG-CAS, using analytical procedures described by Li *et al.* (2006). Sr and rare earth elements (REEs) were separated using cation columns, and Nd fractions were further separated with HDEHP-coated Kef columns. Measured $^{87}Sr/^{86}Sr$ and $^{143}Nd/^{144}Nd$ ratios were normalized to $^{86}Sr/^{88}Sr = 0{\cdot}1194$ and $^{146}Nd/^{144}Nd = 0{\cdot}7219$, respectively. The reported $^{87}Sr/^{86}Sr$ and $^{143}Nd/^{144}Nd$ ratios were adjusted to the NBS SRM 987 standard with $^{87}Sr/^{86}Sr = 0{\cdot}71025$ and the Shin Etsu JNdi-1 standard with $^{143}Nd/^{144}Nd = 0{\cdot}512115$.

RESULTS

Minerals major and trace elements, zircon U–Pb geochronology and HF–O isotopic data, whole-rock major and trace element and Sr–Nd isotope data are included in Supplementary Data Tables S1–S8 (supplementary data are available for downloading at http://www.petrology.oxfordjournals.org).

Mineral chemistry

Clinopyroxene

In hornblende gabbros, clinopyroxene crystals are dominated by a diopside component. In contrast, clinopyroxenes from dolerite and diorite porphyry dykes straddle augite–diopside compositions. Clinopyroxenes show insignificant intra-grain core to rim zoning for all investigated samples. The Mg# decreases with increasing Al_{total}, whereas Ti increases with increasing Al_{total} (Fig. 4a), describing well-defined trends in the gabbro and dolerite dykes that reflect a similar path controlled by olivine + clinopyroxene + amphibole fractionation. In contrast, clinopyroxenes from the diorite porphyry dyke appears as an isolated group recording the effect of plagioclase fractionation.

The chondrite-normalized REE patterns for clinopyroxenes are bell-shaped, showing relative depletions in both light REEs (LREEs) and heavy REEs (HREEs) with respect to middle REEs (MREEs) (Fig. 4b). It is noteworthy that the clinopyroxenes from the diorite porphyry dyke are about 5 times more enriched in REE than those from the hornblende gabbro and dolerite dykes. In addition, the former are characterized by strong negative Eu anomalies ($Eu/Eu^* = 0{\cdot}30–0{\cdot}45$, calculated as $Eu/Eu^*=Eu_N/sqrt(Sm_N*Gd_N)$, normalized to CI) and low Sr contents (34·2–190 ppm), whereas the latter show weak Eu anomalies ($Eu/Eu^* = 0{\cdot}84–1{\cdot}15$) and high Sr contents (72·8–109 ppm) (Supplementary Data Table S1).

All clinopyroxenes from peralkaline granite are calcic–sodic or sodic pyroxenes.

The cores of clinopyroxene phenocrysts, observed in the peralkaline granite, belong to the calcic–sodic pyroxene group of aegirine–augite, whereas the rims of clinopyroxene phenocrysts and late stage clinopyroxenes that replace arfvedsonite are typically aegirine sodic pyroxene. Some clinopyroxene phenocrysts show zoning patterns with dark brown cores surrounded by pale-green rim zones. Compositional variations record abrupt increases in Ti, Na and Fe^{3+} and decreases in Ca, Mn, Fe^{2+}, and Mg abundances from core to rim (Fig. 5).

The chondrite-normalized REE patterns for aegirine–augite and aegirine from peralkaline granites are similar to those reported from other alkaline complexes (Marks *et al.*, 2004). Both aegirine–augite and aegirine are characterized by concave LREE shapes, significant negative Eu anomalies ($Eu/Eu^*=0{\cdot}03–0{\cdot}21$) and pronounced enrichment of HREEs. Aegirine rims are depleted in REE concentrations compared to aegirine–augite cores by three orders of magnitude relative to Chondrite, and aegirine from the rims of arfvedsonite is enriched in HREEs, Nb–Ta and Zr–Hf contents (Fig. 6a,b).

Amphibole

The amphibole classification scheme is based on the International Mineralogical Association (IMA) classification (Hawthorne *et al.*, 2012) and calculated using an excel spreadsheet from Locock (2014) (Supplementary Data Fig. S1). All amphiboles from the gabbro and dolerite dykes and monzogranite are calcic and magnesium rich. Amphiboles from the gabbro and dolerite dykes are primarily pargasite and minor magnesio-hornblende, and most amphiboles from monzogranite are magnesio-hornblendes. Some amphibole rims in the dolerite dyke have high Si and low Mg# similar to those from monzogranite (Fig. 7a).

In the gabbros, amphiboles typically display bell-shaped chondrite-normalized REE patterns with no significant Eu anomalies (0·84–1·0). Amphibole cores from monzogranites also display bell-shaped patterns and the convexity generally increases in rims, which also have stronger Eu anomalies (0·02–0·16 vs 0·38–0·62). In relative terms, amphibole REE concentrations are lowest in the gabbro, intermediate in the cores of crystals in monzogranite and highest in the rims of amphiboles in the monzogranites. The increase in REE contents is coupled with increasing Eu anomalies associated with greater magma differentiation (Fig. 7b).

In the peralkaline granite, both euhedral crystals and subhedral to interstitial amphibole have compositions that are dominantly sodic (arfvedsonite) with minor sodic–calcic amphiboles (katophorite and ferro-richterite). The amphibole phenocrysts in peralkaline granite show compositional zoning from core to rim, where the cores have high Ca and total Al, and lower Na, Ti and K compared to the rims (Fig. 8). The amphibole chondrite-normalized REE patterns are characterized by relatively flat LREE and MREE, marked negative Eu-anomalies ($Eu/Eu^* = 0{\cdot}02–0{\cdot}26$) and enrichment in the HREE (Fig. 6c,d).

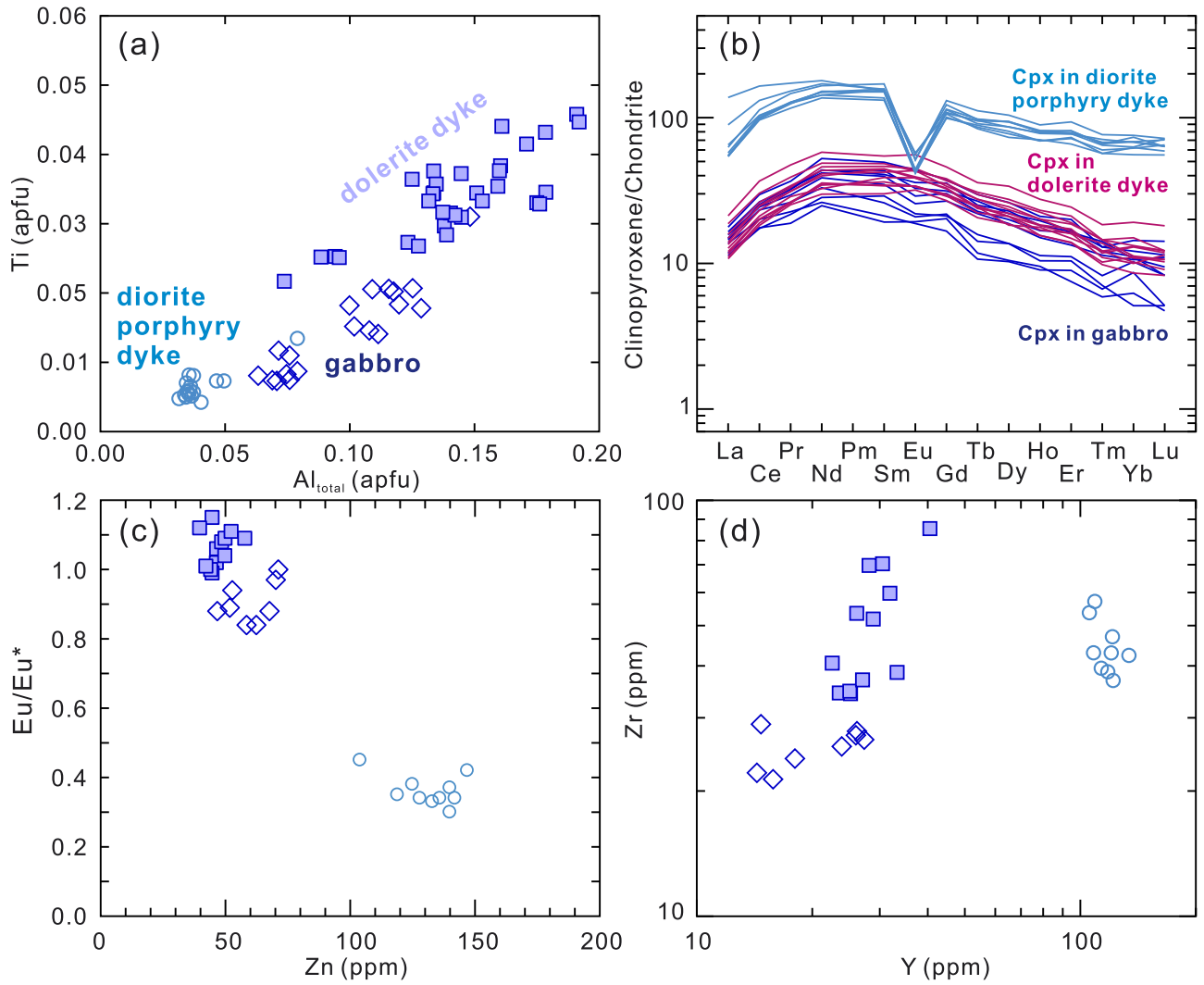

Fig. 4. Clinopyroxene mineral chemistry for the calc-alkaline series (gabbro, dolerite and diorite porphyry dyke). Chondrite normalizing values in (b) are from Sun & McDonough (1989).

Plagioclase

Plagioclases in gabbros are largely unzoned euhedral grains, dominantly ranging from anorthite to bytownite ($An_{94–69}$) in composition. Some crystals are normally zoned with sharp growth zones characterized by lower An contents ($An_{65–35}$). Two types of plagioclase phenocrysts were recognized in the dolerite dykes, including normally zoned plagioclase with andesine cores ($An_{44–41}$) to oligoclase rims ($An_{27–22}$), and oscillatory zoned phenocrysts with high amplitude, high-frequency variations in compositions ($An_{64–12}$). Plagioclases in diorite porphyry dykes are predominantly oscillatory zoned with compositions ranging across $An_{50–12}$. The plagioclase An contents within monzogranites range from andesine to albite ($An_{34–5}$). They host oscillatory zoned plagioclases ($An_{34–8}$), and normally zoned plagioclase with andesine–oligoclase cores ($An_{34–19}$) to oligoclase–albite rims ($An_{15–5}$) (Fig. 9a).

Plagioclase in the calc-alkaline series (gabbro, dolerite and diorite porphyry dykes, monzogranite) defines a trend of decreasing Sr with decreasing An contents, although the monzogranites have relatively uniform Sr across $An_{10–30}$. In contrast, plagioclases show a complex variation of Ba contents with An. Ba generally increases with decreasing An content for gabbro, dolerite and diorite porphyry dykes, but monzogranites show high amplitude variations in Ba concentration that show a negative relationship with An (Fig. 9b,c).

Zircon data

Zircon U–Pb geochronology

Zircon crystals from hornblende gabbro (Sample AET68) are long prismatic and *c.*50 to 300 μm in length, and most show oscillatory zoning (Fig. 10a). The zircons have high Th (595–2850 ppm) and U (1180–5272 ppm) contents and high Th/U ratios (0·3–0·8). Eighteen analyses on 15 grains have $^{206}Pb/^{238}U$ ages from 306 to 322 Ma, with a weighted mean $^{206}Pb/^{238}U$ age of 314·1 ± 4·2 Ma (MSWD = 0·22), which is interpreted as

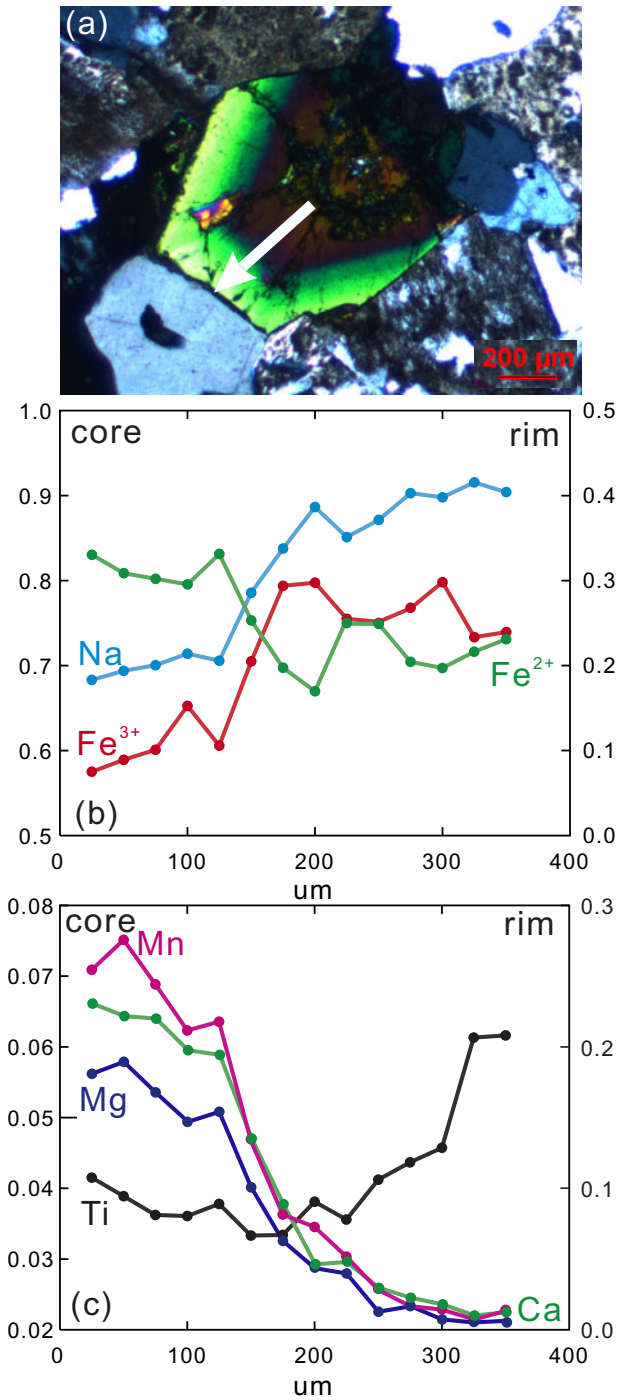

Fig. 5. (a) Typical clinopyroxene phenocryst in the peralkaline granite showing core–rim compositional zoning, the white line shows the location of the profile presented in (b–c). (b–c) core-to-rim profile of mineral chemistry through the zoned, euhedral clinopyroxene crystal shown in (a).

the igneous crystallization age for the gabbro sample (Fig. 10b).

Zircons from a diorite porphyry dyke (Sample AET99) are typically euhedral and small, ranging from *c.*50 to 80 μm in length. Sector zoning or broad oscillatory zoning is common in the zircons (Fig. 10a). They have low concentrations of Th (93–395 ppm) and U (137–348 ppm), with high Th/U ratios (0·5–1·0). Except for one zircon grain that has a $^{206}Pb/^{238}U$ age of 333 Ma, interpreted as a xenocrystic age, nine zircons have $^{206}Pb/^{238}U$ ages of 315 to 325 Ma, yielding a weighted mean $^{206}Pb/^{238}U$ age of 317·5 ± 5·8 Ma (MSWD = 0·21) (Fig.10b).

Zircon crystals from three monzogranite samples (Sample AET77, AET87 and AET95) are euhedral and exhibit numerous narrow oscillatory zones, ranging in size from *c.*100 to 150 μm in length (Fig. 10a). They contain comparable Th (53–1068 ppm) and U (125–11168 ppm) and Th/U = 0·4 –1·4. Zircons AET77, AET87 and AET95 yield weighted mean $^{206}Pb/^{238}U$ ages of 321 ± 4 Ma (MSWD = 0·57; n = 21), 318 ± 4 Ma (MSWD = 0·64; n = 19) and 319 ± 4 Ma (MSWD = 0·67; n = 19), respectively (Fig. 10b).

Zircons from four samples of peralkaline granites (Samples AET63, 08AET82, 08AET86 and107) display a range of features but are dominated by anhedral, sector-zoned cores with fine oscillatory zoning on their rims; they range in size from *c.*80 to 150 μm in length (Fig. 10a). They have variable Th (142–1467 ppm) and U (21–855 ppm) contents and high Th/U ratios (0·3–1·9). Zircon grains from peralkaline granites AET63, 08AET82, 08AET86 and AET107 yield weighted mean $^{206}Pb/^{238}U$ ages of 319 ± 3 Ma (MSWD = 1·04; n = 8), 323 ± 4 Ma (MSWD = 0·92; n = 18), 319 ± 4 Ma (MSWD = 0·92; n = 20), and 320 ± 5 Ma (MSWD = 0·21; n = 6), respectively (Fig. 10b).

Zircon Hf–O isotopes

All samples have high and uniform Hf isotope compositions, with most $\varepsilon_{Hf}(t)$ values between +12 and +16. Zircon grains from the hornblende gabbro and diorite porphyry dyke samples have $\varepsilon_{Hf}(t)$ values of +11·6 to +14·9 and +11·5 to +14·4. Zircon grains from the monzogranites have slightly lower $\varepsilon_{Hf}(t)$ values (+11·2 to +14·8) than the peralkaline granites (+11·6 to +16·8) (Fig. 11a).

The measured zircon $\delta^{18}O$ values for hornblende gabbro (Sample AET68) exhibit a limited range of 5·3 to 5·8‰, averaging 5·6 ± 0·4‰ (2SD). In contrast, the diorite porphyry dyke (Sample AET99) has variable zircon $\delta^{18}O$ values ranging from 4·8 to 6·4, with a mean of 5·5 ± 0·8‰ (2SD). Zircons from three monzogranite samples have higher $\delta^{18}O$ values and larger variations. Those from sample AET77 have a mean oxygen isotope composition of 5·2 ± 0·5‰ (2SD) and range from 4·9 to 5·7 ‰. Zircons from AET87 display a much larger range in $\delta^{18}O$ from 4·5 to 6·5 ‰ and those from sample AET95 have a mean $\delta^{18}O$ value of 6·0 ± 0·9 ‰ (2SD) (Fig. 11a).

The three samples of peralkaline granites have low zircon $\delta^{18}O$ values: sample AET63 show a limited range of between 2·8 and 3·9‰, with a mean value of 3·3 ± 0·5 ‰ (2SD), the $\delta^{18}O$ values of zircons from sample AET82 fall between 3·5 and 4·3‰, with a mean value of 3·9 ± 0·4‰ (2SD), sample AET86 displays a relatively

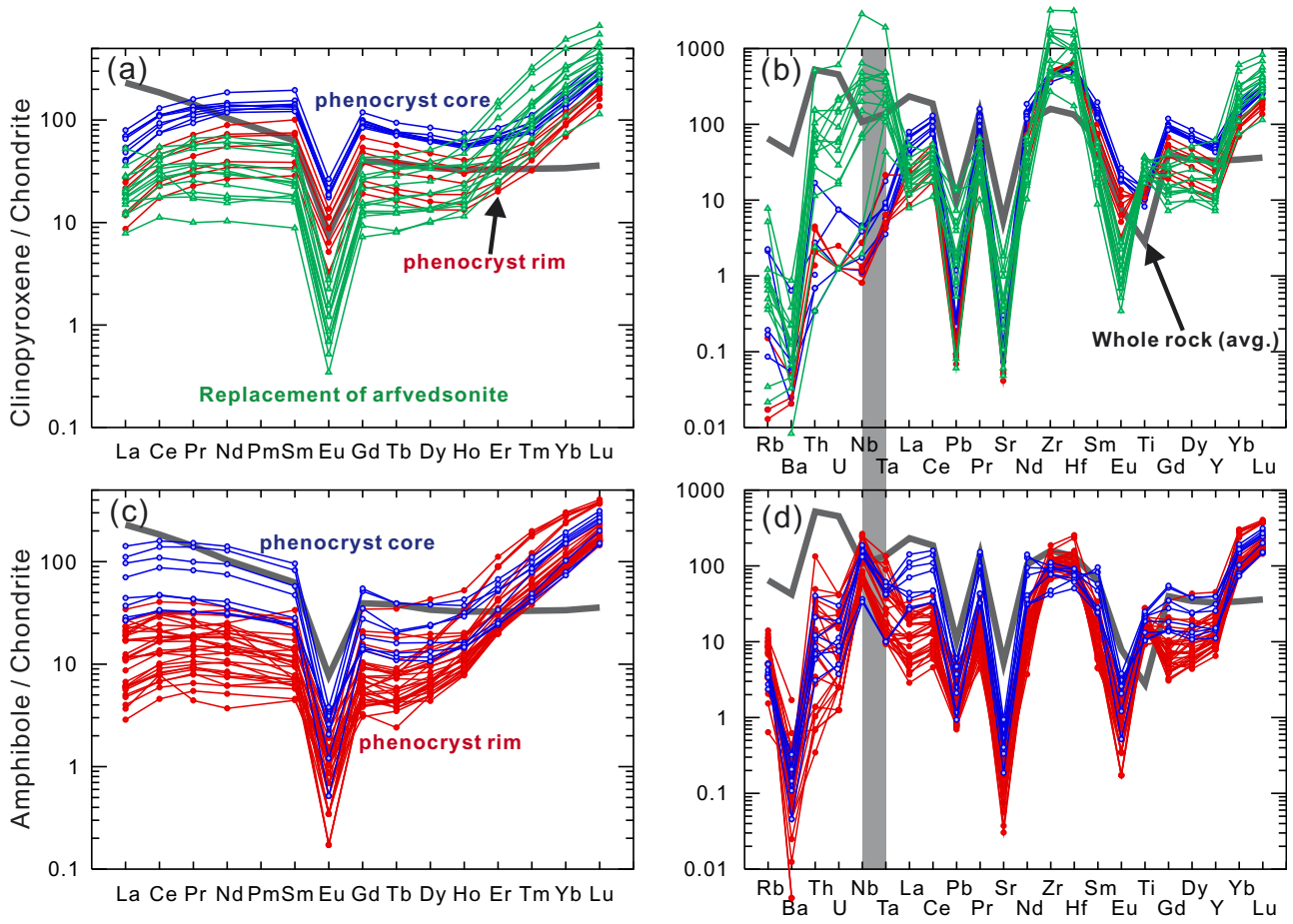

Fig. 6. REE and trace elements of (a, b) clinopyroxenes and (c, d) amphiboles normalized to chondrite (Sun & McDonough, 1989) for the peralkaline series compared with the average whole rock pattern.

large $\delta^{18}O$ variation of between 2·3 and 4·4‰, with a mean value of 3·6 ± 1·0‰ (2SD) (Fig. 11a).

Whole rock major and trace element geochemistry

Two different magmatic series were recognized for the Ulungur intrusive complex (Fig. 12): one is characterized by medium- to high-K calc-alkaline gabbro to monzogranite (North-Tasigake), and the other is defined by peralkaline aegirine–arfvedsonite granite (Saertielieke, Jierdekala and South-Tasigake) (Fig. 12). The calc-alkaline series rocks plot in the gabbro, monzodiorite and monzogranite fields, and the peralkaline series rocks plot in the alkali-feldspar granite field on the QAP diagram (Streckeisen, 1974) (Fig. 12a). On an A/NK vs A/CNK diagram (Maniar & Piccoli, 1989) (Fig. 12d), the calc-alkaline series mafic to intermediate samples have metaluminous characteristics. However, most monzogranites have weak peraluminous signatures (1.0<A/CNK<1.1). On the TAS diagram (Le Maitre, 2002) (Fig. 12b), the calc-alkaline series displays mafic to granitic compositions, extending from gabbro (41.8–46.6 wt.% SiO_2), dolerite dyke (51·1–53·0 wt % SiO_2), diorite porphyry dyke (57·9–64·9 wt % SiO_2), to monzogranite (69·1–76·4 wt % SiO_2). In contrast, the peralkaline series is mostly composed of granitic rocks (73·6–77·4 wt % SiO_2), with the exception of two syenitic granites (67·6–69·4 wt % SiO_2). Samples from both series are compared with other Junggar granitoids on Harker diagrams in Fig. 13 and display clear differentiation trends. The two series define broadly linear, but distinct, trends on most Harker diagrams and display affinities with different Junggar granitoids. The trends demonstrate, therefore, that the Ulungur intrusive complex represents two distinct series of Junggar granitoids.

On chondritic- and primitive mantle-normalized multi-element plots (Sun & McDonough, 1989), the Eu, Nb–Ta, and Ti negative anomalies generally become stronger from gabbro to monzogranite for the calc-alkaline series, although some gabbros and dolerite dykes are characterized by positive Eu anomalies (Fig. 14a). In addition, the intermediate to felsic samples (diorite porphyry dyke and monzogranite) display concave-up shaped patterns. For the peralkaline series, we distinguish two groups: low SiO_2 (67·6–69·4 wt %) and high SiO_2 (73·6–77·4 wt %) samples (Fig. 12b). For all samples, the REEs are strongly enriched relative to chondrite with negative Eu anomalies, and the LREEs are moderately enriched with respect to the HREEs. The low SiO_2 samples (syenitic granites), however, have

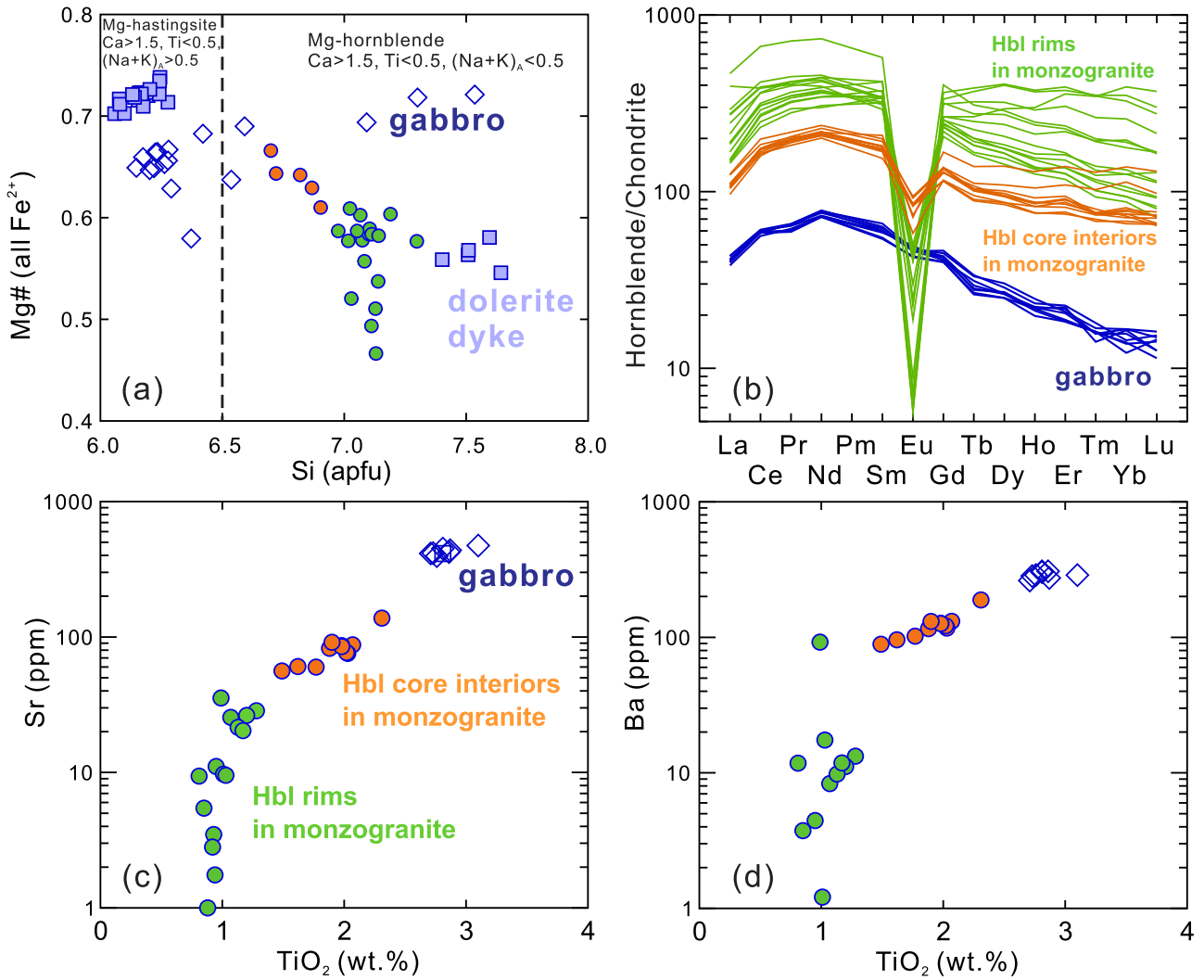

Fig. 7. Amphibole mineral chemistry for the calc-alkaline series (gabbro, dolerite dyke and monzogranite). Chondrite normalizing values in (b) are from Sun & McDonough (1989).

weak Eu and Ba anomalies and lower HREEs compared to the high SiO_2 samples (Fig. 14c,d).

Whole rock Sr–Nd isotopes

The initial Sr–Nd isotopic compositions are calculated to 320 Ma, based on zircon U–Pb dating results obtained by this study. Samples were plotted on an initial $^{87}Sr/^{86}Sr$ vs $\varepsilon_{Nd}(t)$ diagram and compared with East Junggar ophiolites (Fig. 11b). The overall variations in Sr–Nd isotopes for the Ulungur intrusive complex are very small. Calc-alkaline series samples have high positive $\varepsilon_{Nd}(t)$ values ranging from +4·1 to +6·8 and low $(^{87}Sr/^{86}Sr)_i$ ratios ranging from 0·7036 to 0·7046. Peralkaline series samples also display high positive $\varepsilon_{Nd}(t)$ values ranging from +4·6 to +6·3, but have extremely high $^{87}Rb/^{86}Sr$ ratios possibly resulting from fractional crystallization of feldspar, which produces a large uncertainty in their initial Sr isotope values (Jahn *et al.*, 2009). The low $^{87}Rb/^{86}Sr$ (<10) samples yield $(^{87}Sr/^{86}Sr)_i$ ratios ranging from 0·7033 to 0·7050 (Fig. 11b).

DISCUSSION

Magma storage and differentiation conditions

There are differences between mineral assemblages in terms of paragenesis and mineral compositions for the various Ulungur intrusive complex rock types, based on the petrographic observations and mineral chemistry data presented above. These differences reflect variable magma compositions and crystallization conditions in terms of pressure, temperature, water content and other intensive parameters at which magmas were stored and differentiated. In order to constrain crystallization conditions, we use two approaches to estimate pressure and temperature for the investigated rocks: experimental phase relations and mineral thermobarometry as presented in the following section.

Dolerite dyke: hydrous high-pressure crystallization

Clinopyroxene is the first phase to crystallize followed by plagioclase, as indicated by the inclusion of

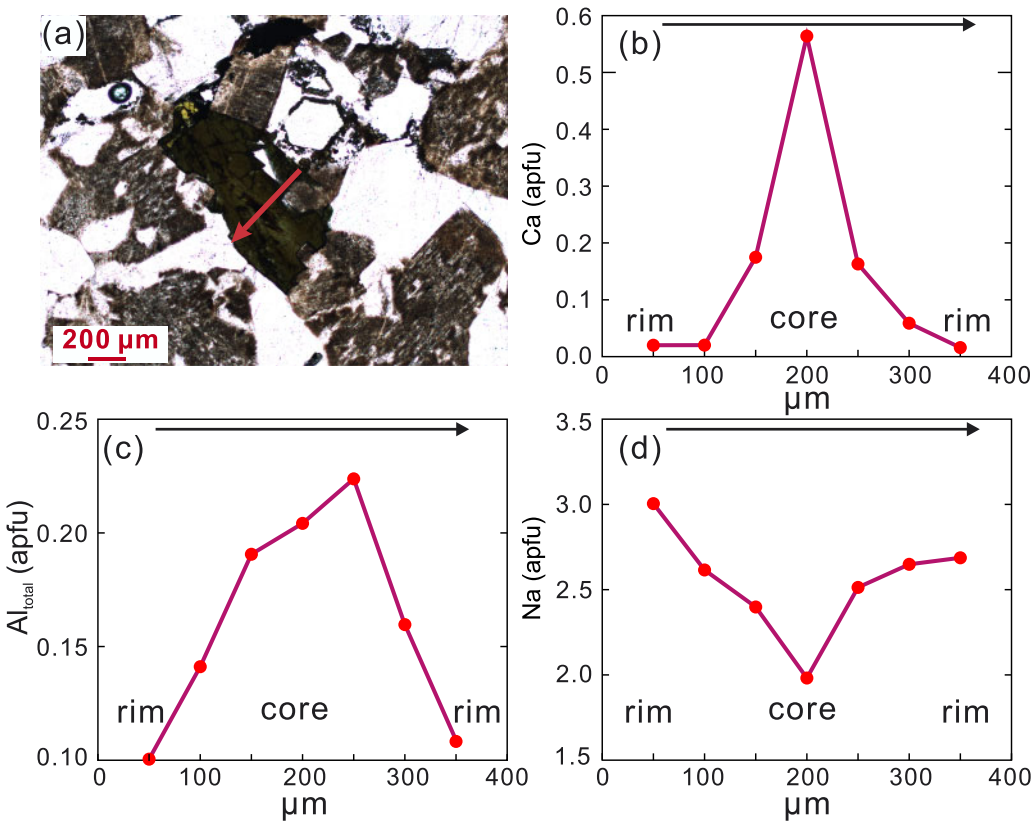

Fig. 8. (a) Typical amphibole phenocrysts in the peralkaline granite showing compositional zoning; the red line indicates the location of the profile given in (b–d). (b–d) core-to-rim profile of mineral chemistry through the zoned, euhedral amphibole crystal shown in (a).

clinopyroxene in larger plagioclase crystals (Fig. 3d,e). Clinopyroxenes are characterized by a lack of Eu anomaly (Eu/Eu* = 1·0–1·1) (Fig. 4b), which also indicates that clinopyroxene crystallized earlier than plagioclase. The Al_2O_3 content increases with decreasing Mg# in clinopyroxene, suggesting suppression of plagioclase crystallization (Müntener *et al.*, 2001; Klaver *et al.*, 2017) (Fig. 15a). Amphibole is also an early crystallizing phase, as indicated by its high Mg# (0·70–0·74) (Fig. 15b), and it accompanied plagioclase crystallization. Experimental studies indicate that at a pressure of 0·7 GPa and initial water content $\geq$ 3 wt % (Blatter *et al.*, 2013; Nandedkar *et al.*, 2014; Melekhova *et al.*, 2015), clinopyroxene and amphibole crystallize in primitive arc magmas and their compositional features are similar to those of the dolerite dyke, including high Al_2O_3 content in clinopyroxene and high Mg# and Al^{VI} contents for amphibole (Fig. 15a,b). Thus, we suggest that the dolerite dykes crystallized from primitive hydrous melts ($\geq$ 3 wt % H_2O) at high-pressure in the lower crust (*c.*700 MPa). It is important to note that some amphibole crystals show an abrupt shift in Al_2O_3 content at the core-rim boundary (Fig. 3e). The amphibole rims in the dolerite dyke have distinctly lower Al_2O_3 and Mg# values comparable to those from amphibole in monzogranite (Supplementary Data Table S2), and thus we infer that these rims crystallized at shallow levels of emplacement (*c.*200 MPa), similar to the monzogranites (see discussion below). In conclusion, the mineral assemblage indicates that the dolerite dyke was derived from primitive hydrous melts crystallized at lower crustal pressures prior to emplacement at shallower levels.

Hornblende gabbro: water-saturated shallow crystallization

The hornblende gabbro commonly contains relict clinopyroxene surrounded by hornblende (Fig. 3b), which indicates a reaction between clinopyroxene and differentiated melt to form hornblende (Smith, 2014) and that the clinopyroxene crystallized earlier than hornblende. In addition, some plagioclases occur as inclusions in clinopyroxene grains (Fig. 3a). These observations show that plagioclase appeared before clinopyroxene, as also evidenced by negative Eu anomalies of the latter (Fig. 4b), and further indicate that clinopyroxene appeared before hornblende in the parental magmas. Thus, the inferred sequence of crystallization is plagioclase → clinopyroxene → hornblende. The hornblende gabbros are characterized by the occurrence of calcic plagioclase ($An_{\leq 94}$) (Fig. 9a), which reflects crystallization from a parental melt under water-rich conditions (Sisson & Grove, 1993; Müntener *et al.*, 2001; Takagi *et al.*, 2005; Nandedkar *et al.*, 2014; Melekhova *et al.*, 2015; Nandedkar *et al.*, 2016). Furthermore, clinopyroxenes show relatively evolved geochemical features

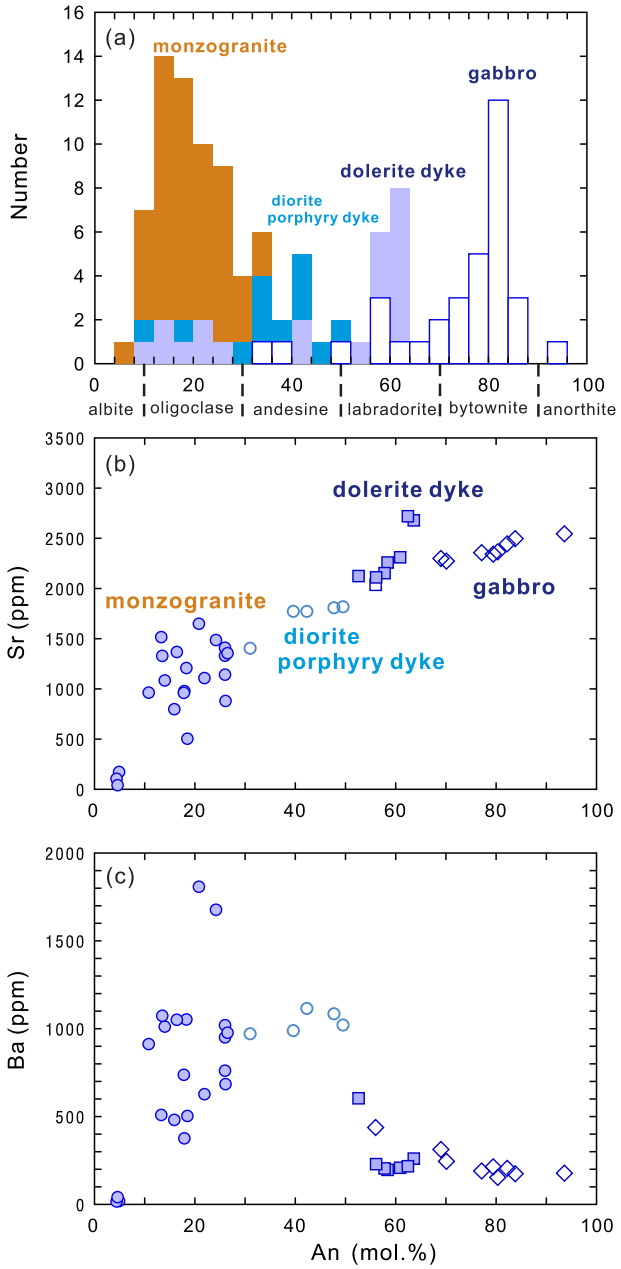

Fig. 9. Histogram of (a) plagioclase An values and (b–c) Sr and Ba vs plagioclase An diagrams for the calc-alkaline series.

(Mg# 0·75–078, < 1000 ppm Cr) (Fig. 15a), which reflect their crystallization from an already differentiated basaltic-andesitic parental melt with low Mg#.

Experimental studies, addressing water-saturated melting for basaltic andesite to andesite melt compositions indicate that early crystallization of plagioclase before clinopyroxene and amphibole occurs at pressures < 300 MPa at about 970 °C (Moore & Carmichael, 1998; Krawczynski *et al.*, 2012). Thus, the hornblende gabbro crystallized at low temperature and pressure conditions. This conclusion is also supported by crystallization experiments at 200 MPa that reproduce the co-occurrence of calcic plagioclase and evolved clinopyroxene using mildly evolved (Mg# = 0·60) starting compositions under H_2O-saturated conditions (Sisson & Grove, 1993). In addition, the hornblendes have lower Mg# (< 0·72) and Al^{VI} contents (< 0·3 apfu) (Fig. 15a-b), which is consistent with crystallization experiments undertaken at lower pressure (200–400 MPa) (Pichavant *et al.*, 2002; Pichavant & Macdonald, 2007; Andujar *et al.*, 2015). Therefore, the hornblende gabbros most likely crystallized from hydrous, mildly evolved basaltic–andesitic melts. Calcic plagioclase crystallized at shallow levels in the crust when the melts reached water saturation (Sisson & Grove, 1993).

Intermediate to felsic samples (diorite porphyry dyke and monzogranite): shallow level crystallization

Clinopyroxene and hornblende from intermediate to felsic samples (diorite porphyry dyke and monzogranite) are characterized by pronounced negative Eu anomalies, indicating that plagioclase was an early crystallizing phase. This interpretation is supported by the petrological observation that plagioclase occurs as inclusions in clinopyroxene (Fig. 3f). Alkali feldspar, biotite and quartz occur as late interstitial crystallizing phases. Thus, the inferred sequence of crystallization is plagioclase → clinopyroxene ± hornblende → alkali feldspar + biotite + quartz. REE concentrations in clinopyroxene and hornblende from the intermediate to felsic samples are higher than those from the dolerite dyke and gabbro, indicating that they crystallized from a differentiated intermediate to felsic melt at lower temperature (Sisson & Grove, 1993). Compared with their gabbro counterparts, plagioclases from the intermediate to felsic samples have lower An values (Fig. 9a) and clinopyroxenes have lower CaO contents (Supplementary Data Table S1). These results indicate that assemblages in the intermediate to felsic samples probably crystallized at lower pressure and water contents relative to those of the gabbros. In addition, clinopyroxenes have lower Al_2O_3 contents (< 1 wt %) and hornblendes have lower Al^{VI} contents (<0.1 apfu) (Fig. 15b). According to experimental results, clinopyroxene and hornblende in the intermediate to felsic samples crystallized from hydrous melts (2–4 wt % H_2O) at shallow levels in the crust (Sisson & Grove, 1993; Nandedkar *et al.*, 2016).

Similar to the gabbro, the intermediate to felsic samples are characterized by the early appearance of plagioclase with respect to clinopyroxene and hornblende. We applied the same approach as for gabbro and our results show that intermediate to felsic samples crystallized from hydrous melts at low pressures (< 300 MPa), and temperatures ranging from 970 °C to 750 °C. To estimate the crystallization conditions, we applied the Al-in-hornblende barometer of Mutch *et al.* (2016). This barometer can only be used for a low thermodynamic variance mineral assemblage (Anderson *et al.*, 2008). Only monzogranites with the complete equilibrium buffering assemblage

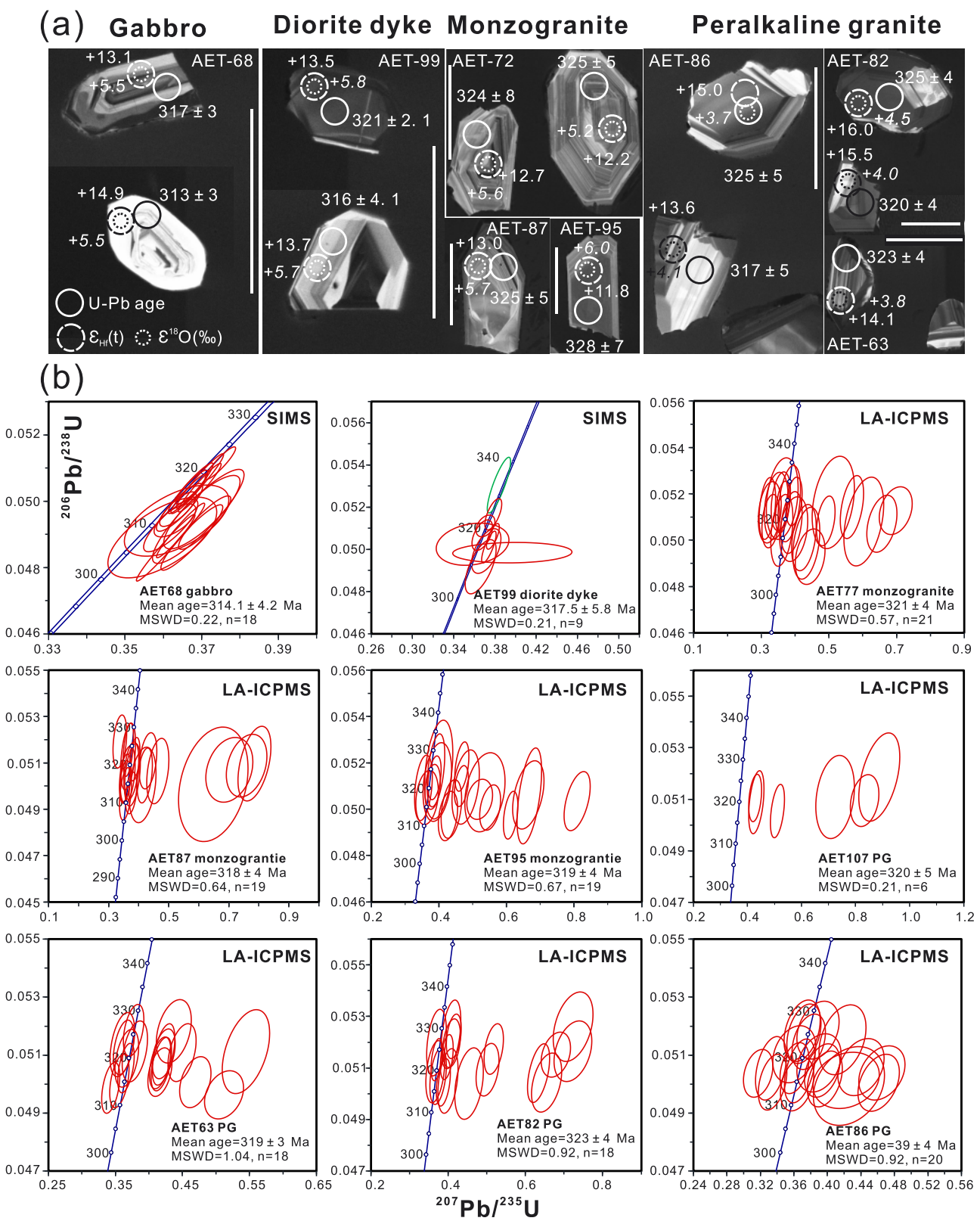

Fig. 10. (a) Cathodoluminescence (CL) images of selected zircon grains highlighting their internal zoning features, and the locations of in situ isotopic analysis. The relative locations of areas analysed by the different techniques (SIMS and LA-MC-ICPMS) are also indicated. The U–Pb ages are presented as $^{206}Pb/^{238}U$ ages for the individual zircon grains and the errors are quoted at the 2SD level. (b) Concordia diagrams of zircon U–Pb dating. PG-peralkaline granitoid. Green ellipse excluded from age determination.

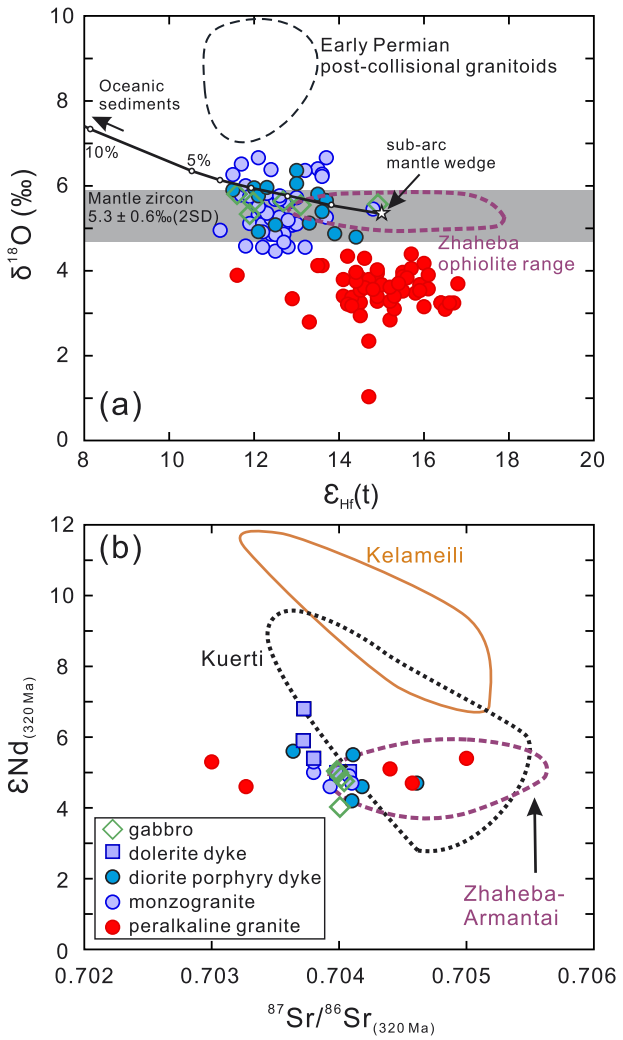

Fig. 11. (a) Plot of $\delta^{18}O$ values vs zircon $\varepsilon_{Hf}(t)$ for the Ulungur intrusive complex. The zircon $\delta^{18}O$ values for mantle and Zhaheba ophiolite are shown for comparision, data are from Valley *et al.* (1998) and Ye *et al.* (2017), respectively. The zircon $\delta^{18}O$ values for the Early Permian post-collisional granitoids are from Tang *et al.* (2019). The curves denote two component mixing trends between the sub-arc mantle wedge and oceanic sediment. Mantle source has $\varepsilon_{Hf}(t) = 15{\cdot}0$ and $\delta^{18}O = +5{\cdot}3‰$; oceanic sediment sediment has $\varepsilon_{Hf}(t) = +2{\cdot}0$ and $\delta^{18}O = +20‰$. Assumed proportions of Hf concentration of oceanic sediment to depleted mantle is 10:1. (b) $\varepsilon_{Nd}(t)$ vs $(^{87}Sr/^{86}Sr)_i$ diagram, East Junggar ophiolites are shown for comparision, data sources are from Liu *et al.* (2017), Ye *et al.* (2017), Shen *et al.* (2018) and references therein.

(plagioclase, amphibole, biotite, alkali feldspar, quartz, magnetite, titanite and apatite) are suitable for barometry. They yield pressures between 128 and 280 MPa, corresponding to mid- to upper-crustal conditions. Temperatures were estimated using the Ti-in-zircon (T_{Ti-Zr}) thermometer from the equations of Ferry & Watson (2007). Following the recommendations of Ferry & Watson (2007), $\alpha TiO_2 = 0{\cdot}7$ and $\alpha SiO_2 = 0{\cdot}7$ are assumed for the monzogranites, and the estimated temperatures range from 988 °C to 665 °C (Supplementary Data Table S5). The calculated pressure–temperature results are also in agreement with the inferred range of pressure conditions based on experimental phase relations (Fig. 15d).

Peralkaline granites: water-rich shallow crystallization

All Ulungur peralkaline granites contain Na-rich aegirine and arfvedsonite, which were considered unsuitable for thermobarometry. We suggest that formation of the peralkaline granite occurred at shallow levels in the crust similar to the calc-alkaline series intermediate to felsic rocks based on the following evidence: 1) the ages between neighboring peralkaline granite and monzogranite and diorite porphyry dyke are within analytical error (Fig. 10b); and 2) the peralkaline granite plutons were intruded by diorite and monzogranite porphyry dykes (Figs 1d and 2b). This inference is also supported by the results of phase equilibrium experiments (Scaillet & Macdonald, 2001, 2006) that reproduce the observed mineral assemblages of the Ulungur peralkaline granite, which suggests that the pressure of magma storage or crystallization for the peralkaline magmas was about 150 MPa. Specifically, the aegirine and arfvedsonite reproduced by these experiments at a pressure of 150 MPa and $>$ 4 wt % H_2O in the melt show similar compositional features to those of the Ulungur peralkaline granite, such as high F content (2·0 ± 1·1 wt %) in arfvedsonite (Supplementary Data Table S2). The high F content allows arfvedsonite to be more stable at lower pressures (Scaillet *et al.*, 2016). These mineral assemblages and compositions suggest that Ulungur peralkaline magma was water-rich (4–6 wt % H_2O) (Scaillet & Macdonald, 2006). Using the same activities of SiO_2 and TiO_2 in the parental melt for monzogranite, temperatures were estimated using the T_{Ti-Zr} thermometer following the equations of Ferry & Watson (2007), which yielded temperatures that range from 1002 °C to 661 °C, but mostly below 850 °C (Supplementary Data Table S2).

Magma source and evolution of calc-alkaline series

Isotopic constraints on the magmatic source: sub-arc mantle wedge

The $\delta^{18}O$ values of zircons from the Ulungur calc-alkaline series samples range from 4·5 to 6·7 ‰ and straddle the field of mantle zircon (Fig. 11a). The mantle-like $\delta^{18}O$ values in zircon, combined with the strongly positive $\varepsilon_{Hf}(t)$ values close to that of mantle-derived melts (Fig. 11a), suggest that the sources of the calc-alkaline series included only minor amounts of supracrustal materials. The absence of inherited zircons in the calc-alkaline series also argues for little to no crustal contamination (Fig. 10). This interpretation is supported by the depleted Sr–Nd isotope compositions of the calc-alkaline rocks and the fact that their Sr–Nd–Hf–O isotope compositions are almost identical to those of the neighboring Zhaheba–Armantai ophiolites (Fig. 11b). These first-order observations suggest that

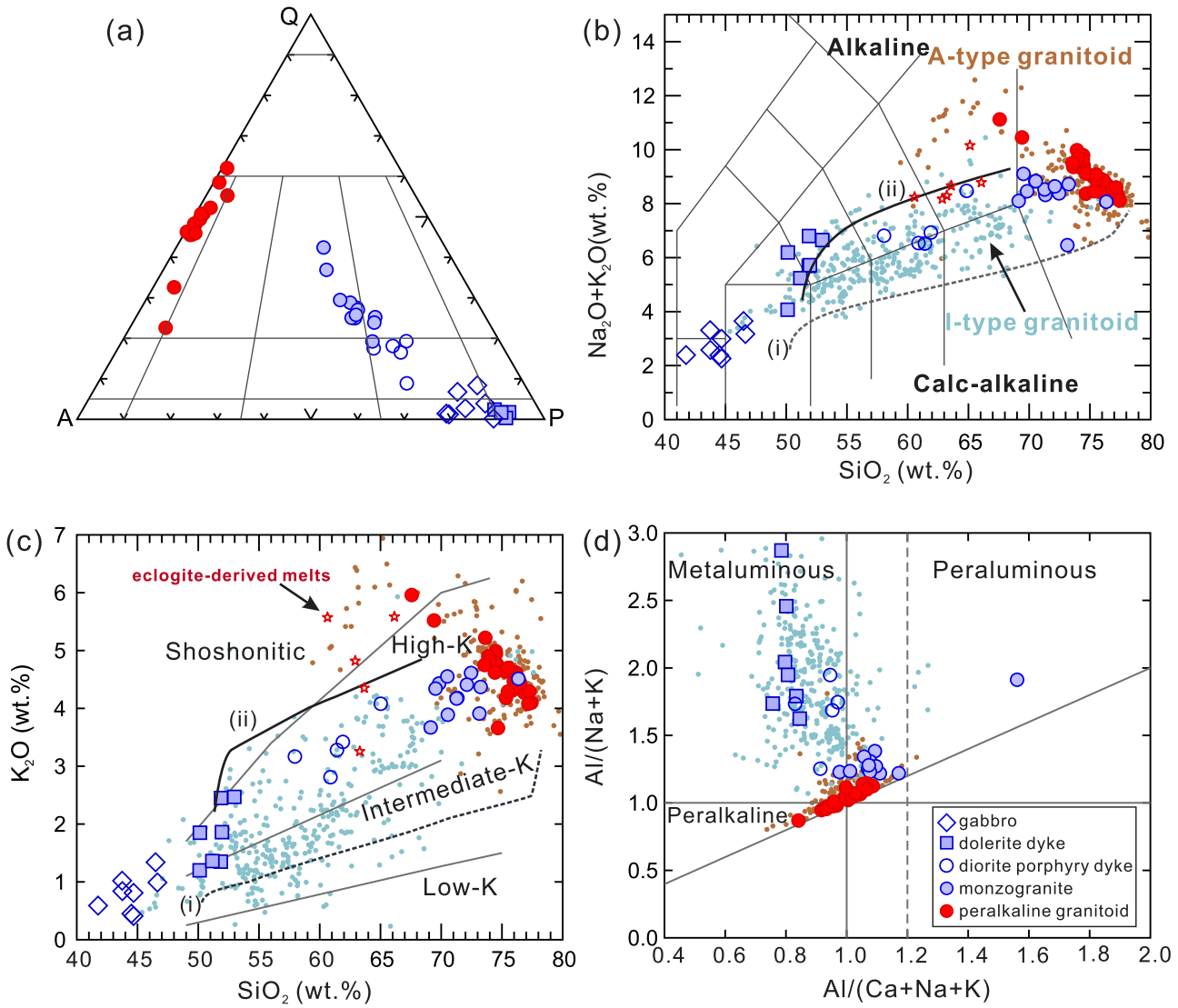

Fig. 12. Whole-rock geochemical characteristics of the Ulungur intrusive complex. (a) QAP for intrusive rocks classification diagram (Streckeisen, 1974). (b) Total alkalis vs SiO_2 (TAS) diagram (Le Maitre, 2002). (c) K_2O vs SiO_2 diagram (Peccerillo & Taylor, 1976). (d) A/NK [molar ratio $Al_2O_3/(Na_2O+K_2O)$] vs A/CNK molar ratio [$Al_2O_3/(CaO+Na_2O+K_2O)$] (Shand, 1943). Data for other Junggar I- and A-type granitoids are from Tang *et al.* (2017a). LLD paths in (b–c) are from fractional crystallization experiments conducted on a primitive hydrous arc magma at 0·7 GPa and temperatures ranging from 1170 to 700 °C (line i; Nandedkar *et al.*, 2014) and from the field-based mass-balance fractionation model in the Dariv igneous complex exposed in Western Mongolia, CAOB (line ii; Bucholz *et al.*, 2014). Eclogite-derived melts (Spandler *et al.*, 2007) are shown for comparison.

the parental magma of the Ulungur calc-alkaline series was derived from the sub-arc mantle wedge with only minor crustal input, which could have been derived via subduction erosion or the subduction of sediments. The addition of minor crustal materials can account for $\varepsilon_{Hf}(t)$ values that are slightly lower than pristine mantle-derived melts, and the slighted elevated $\delta^{18}O$ values in zircons in comparison to purely mantle-derived zircons. Therefore, the most plausible crustal addition to the melt source region is oceanic sediments, which have high $\delta^{18}O$ values and low $\varepsilon_{Hf}(t)$ values. A simple binary mixing model suggests that a maximum addition of 5% oceanic sediments to the source of the calc-alkaline series magmas could account for their slightly lower $\varepsilon_{Hf}(t)$ values and the occurrence of some zircons with slightly elevated $\delta^{18}O$ values (Fig. 11a). Our calculated amount of oceanic sediment input is consistent with the results for arc peridotite xenoliths that record a similar contribution of *c.*5% slab-derived material into the mantle wedge (Chin *et al.*, 2014).

The gabbros are interpreted as cumulates due to their cumulate texture and very low SiO_2 contents (41·8–46·6 wt %). Intermediate to felsic samples, displaying higher SiO_2 contents (> 57·9 wt %), are interpreted as differentiated rocks, whereas the dolerite dykes are assumed to approximate parental melt composition for the differentiated calc-alkaline series, although their low Mg#'s (< 0·52) (Fig. 13a) indicate that they are not primary, but derived from mantle melts that experienced some crustal differentiation. The

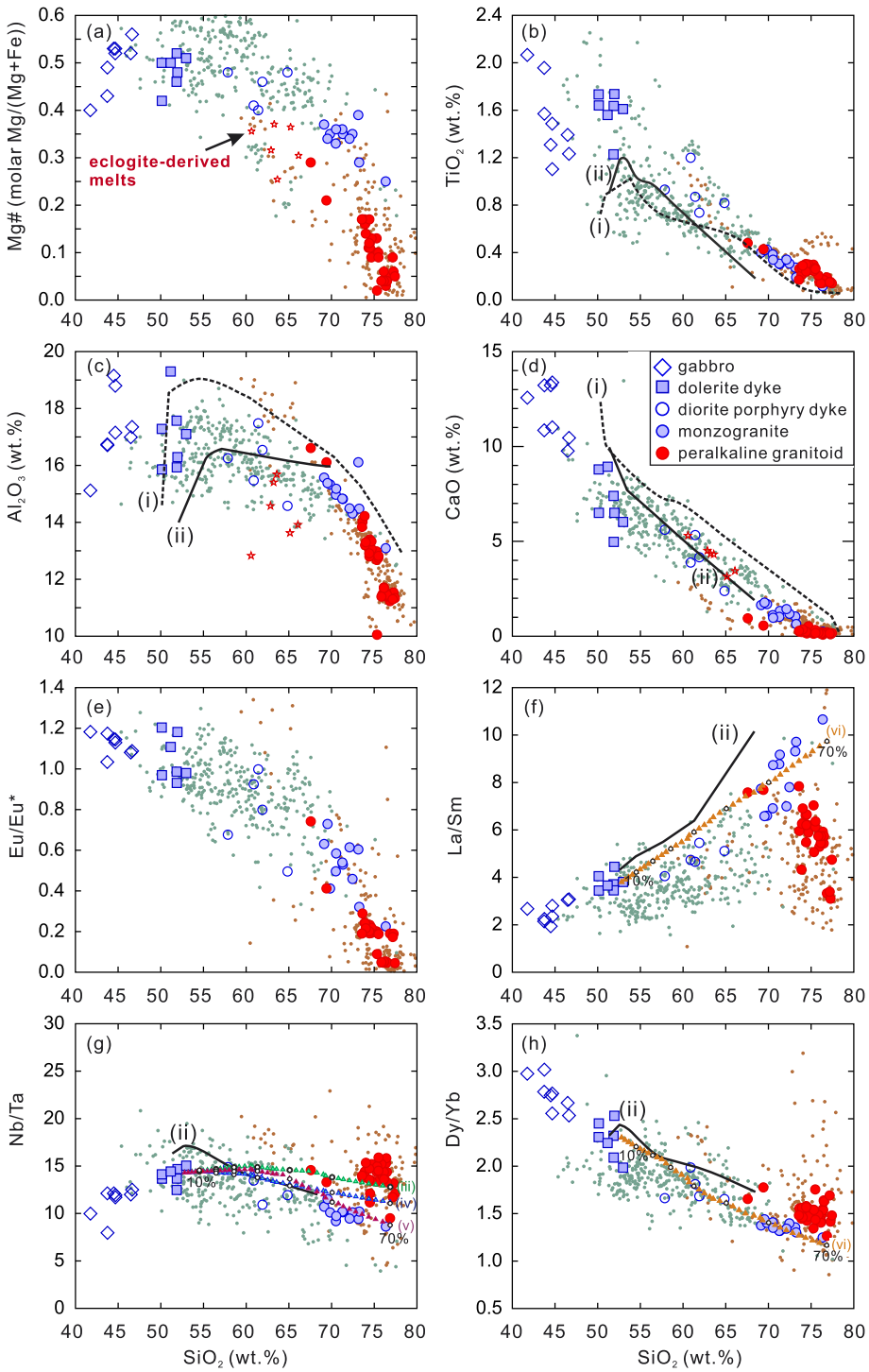

Fig. 13. Harker diagrams illustrating the variation of major elements (Mg#, TiO_2, Al_2O_3, CaO) and trace element ratios (La/Sm, Nb/Ta, and Dy/Yb) vs SiO_2. Simple models of crystal fractionation are shown on (f–h), and modelling parameters and results are listed in Supplementary Data Table S10. On panel (g), model (iii): hornblende only; model (iv): hornblende + plagioclase in proportions as in experiments of Nandedkar *et al.* (2014), joined by 5% biotite at 55 wt % SiO_2, and model (v) as model (iv), but joined by 50% plagioclase and 50% biotite at 65 wt % SiO_2. SiO_2 vs La/Sm and Dy/Yb (f and h, model vi): modelling results are shown for crystallization of amphibole + plagioclase ± apatite in proportions as in experiments of Nandedkar *et al.* (2014). The small circles on the modelling curves represent accumulated solid fraction. Symbols and LLD are as in Fig. 12.

chondrite-normalized $[Gd/Yb]_N$ ratios for dolerite dykes range between 1·9 and 2·9, indicating the presence of garnet in the mantle source region. Using the non-modal batch melting model (Shaw, 2000) (Supplementary Data Fig. S2), we modeled the melting of garnet lherzolites on REE patterns to illuminate the source mineralogy and mantle melting history of the dolerite dykes. In addition, Rayleigh fractionation of

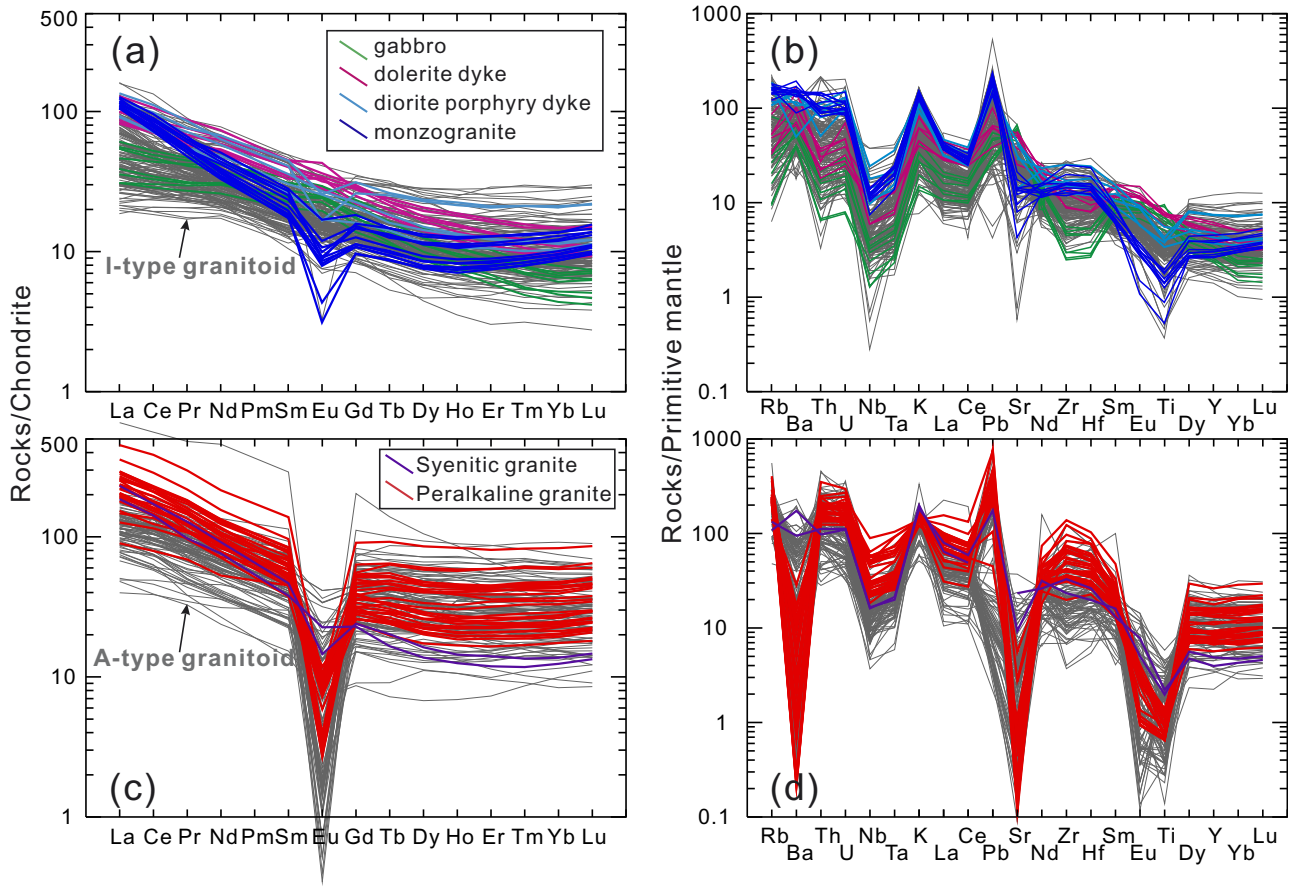

Fig. 14. Whole rock chondrite-normalized REE patterns (a and c) and Primitive Mantle-normalized trace element variation (b and d) diagrams for the Ulungur intrusive complex, and other Junggar granitoids (Tang *et al.*, 2017a) shown for comparison. Chondrite and Primitive Mantle normalizing values are from Sun & McDonough (1989).

ultramafic rocks was modeled in order to reproduce the parental melt compositions corresponding to those observed in the dolerite dykes. Model parameters, partition coefficients and all calculations are provided in Supplementary Data Table S9. The model results show that the REE pattern for the dolerite parental magma is best reproduced by a moderate degree ($F = 0{\cdot}05$) of melting a garnet lherzolite (2% garnet), using a depleted MORB mantle (DMM) with 10% altered oceanic crust (AOC) melt as the magma source, and followed by 10–40% early fractionation of olivine-rich ultramafic cumulates. The early fractionation of olivine-rich ultramafic cumulates may also explain the low Mg# values of the dolerite dykes (Supplementary Data Fig. S2).

Magma differentiation dominated by crustal fractional crystallization

Plagioclase fractionation is supported by decreasing Sr content with decreasing plagioclase An in the calc-alkaline series (Fig. 9b). In the monzogranites, Ba decreases with decreasing An in plagioclase (Fig. 9b). The trend corresponds to crystallization of alkali feldspar and biotite because these phases contain high Ba concentrations (e.g. biotite, Ba > 2930 ppm) (Supplementary Data Table S3). The Eu/Eu* vs Zn diagram shows that clinopyroxenes from dolerite dyke and gabbro are characterized by negligible Eu anomalies with low Zn contents (Fig. 4c), corresponding to the fractionation of mafic mineral phases, but not plagioclase. This inference is consistent with the positive correlation between Ti and Al_{tot} for clinopyroxenes in these rocks (Fig. 4a). In contrast, the low Al_{tot} content, high Zn concentration and distinctly negative Eu anomalies of the clinopyroxenes from the diorite porphyry dyke indicate clinopyroxene and plagioclase co-saturation from andesitic magmas (Fig. 4). The onset of plagioclase crystallization would decrease the activity of Ca in the melt, thus favoring Zn incorporation into the crystal lattice of clinopyroxenes in the diorite porphyry dyke (Gori *et al.*, 2015). Hornblende Ti, Sr and Ba concentrations decrease from interiors to rims in monzogranites (Fig. 7a,b), indicating fractionation of hornblende along with plagioclase, alkali feldspar, Fe–Ti oxides, and biotite (Barnes *et al.*, 2016). Furthermore, hornblende interiors and rims in the monzogranites show different trends on Sr and Ba vs TiO_2 diagrams (Fig. 7c,d). The strong decrease in Sr and Ba contents for hornblende rims, compared to a more moderate decrease for interiors, suggests that continued fractionation of

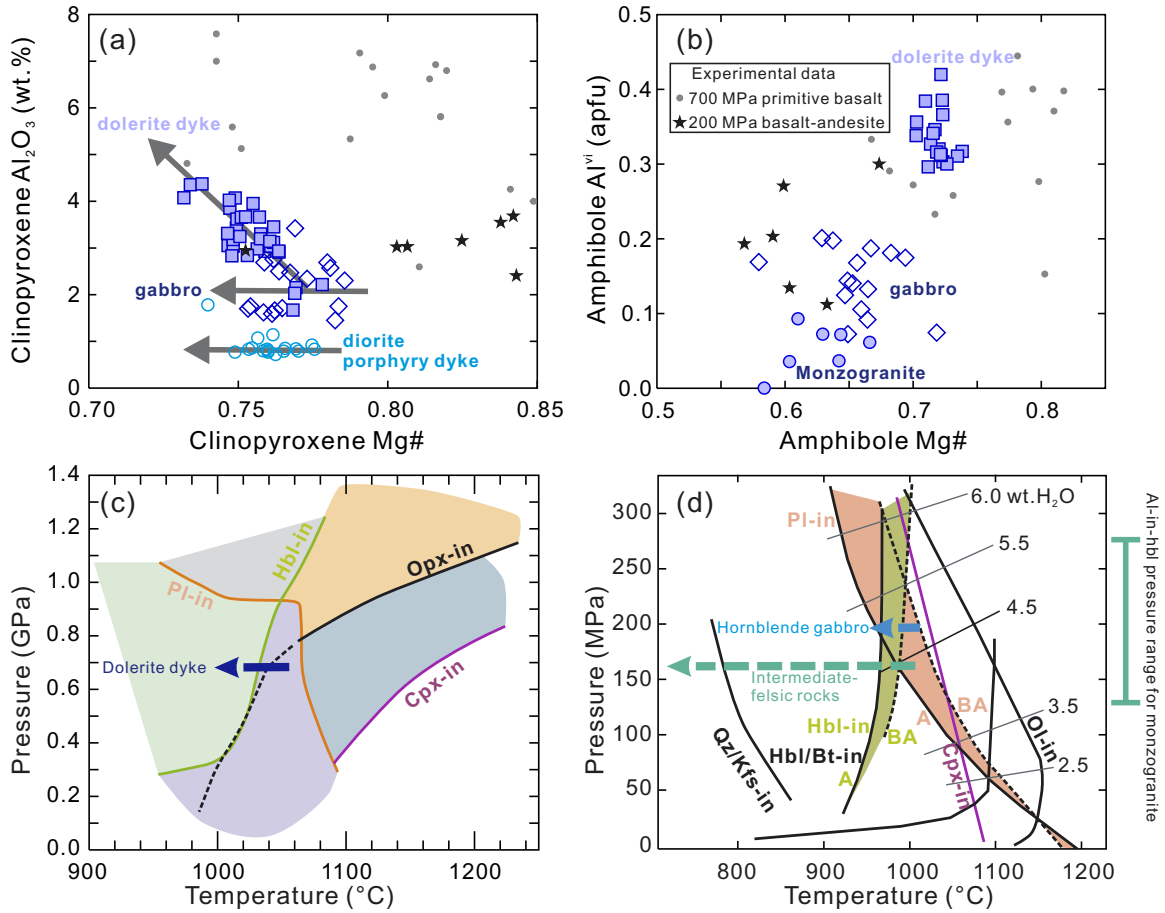

Fig. 15. (a) Clinopyroxene Al_2O_3 content vs Mg#; (b) Amphibole Al^{VI} vs Mg#. Grey dot and black star represent the results of crystallization experiments for primitive basalt at 700 MPa (Blatter *et al.*, 2013; Nandedkar *et al.*, 2014; Melekhova *et al.*, 2015) and basalt–andesite at 200–400 MPa (Sisson & Grove, 1993; Grove *et al.*, 2003; Andujar *et al.*, 2015, 2016), repectively. (c) Phase diagram for the hydrous ($\geq$ 3 wt % H_2O) starting material of primitive arc magmas (Klaver *et al.*, 2017). The dolerite dyke is consistent with crystallisation at *c.*700 MPa. (d) Phase diagram for hydrous (3–5 wt % H_2O) basaltic-andesite (BA) and andesite (A) starting compositions after Moore & Carmichael (1998). Biotite and quartz–K-feldspar are from Righter & Carmichael (1996) and Rutherford & Devine (2003), respectively. See text for discussion.

hornblende was accompanied by progressively more alkali feldspar and biotite crystallization.

The liquid line of descent (LLD) obtained from fractional crystallization experiments conducted on primitive hydrous arc magmas at 700 MPa and temperatures ranging from 1170 to 700 °C (Nandedkar *et al.*, 2014), and from the field-based mass-balance fractionation model for the Dariv igneous complex of Western Mongolia, CAOB (Bucholz *et al.*, 2014), are compared with the major and trace element differentiation trends recognized in Ulungur calc-alkaline series rocks in Figs 12 and 13. The differentiation trends of the calc-alkaline series do not closely follow the LLDs. The reason, at least in part, is likely the strongly porphyritic nature of many rock types (Fig. 2). Differences in the sources of the Ulungur magmas vs the modelled rocks may also be a factor. Consequently, adopting the method of Müntener *et al.* (2018), we used crystal fractionation modeling to illustrate the evolution of Nb/Ta, Dy/Yb and La/Sm ratios of fractionating calc-alkaline magmas, based on fractional crystallization experiments (Nandedkar *et al.*, 2014; 2016) (Fig. 3f–h). Detailed calculations and mineral partition coefficient values are summarized in Supplementary Data Table S10.

The Ulungur calc-alkaline series is characterized by generally decreasing Nb/Ta with increasing SiO_2 (Fig. 13g), which is a trend recognized in arc magmas globally (Müntener *et al.*, 2018). Nb and Ta are moderately incompatible in amphibole, and compatible in biotite in calc-alkaline compositions (Acosta-Vigil et al., 2010; Nandedkar *et al.*, 2016), and ratios of mineral/liquid partition coefficients D_{Nb}/D_{Ta} are generally >1 (Müntener *et al.*, 2018) (Supplementary Data Table S10). For the Ulungur calc-alkaline series, amphibole and biotite are the two major Nb-Ta enriched minerals and both have higher Nb/Ta ratios ($>$ 20) than the whole rocks ($<$ 15) (Supplementary Data Tables S2 and S4). Therefore, crystallization of amphibole and biotite would deplete Nb in melt and decrease the Nb/Ta ratio of the residual melt. The decrease of TiO_2 with increasing SiO_2 (Fig. 13b), combined with a typical REE concave-up shape (Fig. 14a), also indicate an important

role for amphibole fractionation (Davidson *et al.*, 2007). Our modelling results show that amphibole along with biotite fractionation can reproduce the decrease of Nb/Ta ratios to below 10, which is consistent with the Ulungur calc-alkaline series. However, amphibole fractionation alone cannot produce the low Nb/Ta ratios of the calc-alkaline series (Fig. 13g). We also modelled Dy/Yb and La/Sm ratios of fractionating calc-alkaline magmas in a similar way, applying the phase proportions and compositions of Nandedkar *et al.* (2014). The result shows that decreasing Dy/Yb and increasing La/Sm with increasing SiO_2 can be reproduced by fractionation of amphibole ± plagioclase and apatite (Fig. 13f and h). Such trends are similar to the LLDs of K-rich arc rocks of the Dariv igneous complex in Mongolia (Bucholz *et al.*, 2014), and modelling results for calc-alkaline magmas (Müntener *et al.*, 2018). In conclusion, the Ulungur calc-alkaline series rocks were derived from magma sources similar to other magmas derived from a depleted sub-arc mantle wedge and the magmas evolved via substantial crustal fractional crystallization.

Magma source and evolution of the peralkaline series

Primary low $\delta^{18}O$ values in zircon: residual oceanic crust in Junggar intra-oceanic arc lower crust

The peralkaline granites are characterized by low zircon $\delta^{18}O$ values and display an average value of 3·6‰, which is lower than the 5·3 ± 0.6‰ range for zircon in the normal mantle (Valley *et al.*, 1998) (Fig. 11a). Zircon can undergo oxygen isotope exchange by post-magmatic zircon-fluid interaction (Gao *et al.*, 2014), although it is insensitive to hydrothermal alteration and fractional crystallization (Valley, 2003). For example, although some A-type granites were considered to be 'low $\delta^{18}O$' when bulk zircon samples are analysed using the laser-fluorination technique (Wei *et al.*, 2008), SIMS in situ oxygen-isotope analyses showed mantle-like $\delta^{18}O$ values; the lower $\delta^{18}O$ values of high-U zircons likely reflect the effects of radiation damage (Gao *et al.*, 2014). It is, therefore, important to evaluate whether the zircon grains preserved primary magmatic oxygen isotopic compositions prior to discussing the origin of the granites. The following lines of evidence suggest that the zircons from Ulungur granites have preserved primary magmatic signatures: 1) Zircon crystals from peralkaline granites show clear oscillatory zoning (Fig. 10a), display moderate Th (mostly < 800 ppm) and U (< 900 ppm) contents and give concordant to nearly concordant U–Pb ages (Fig. 10b); 2) Zircon crystals from each sample with high Th/U ratios have restricted oxygen isotopic compositions and zircon $\delta^{18}O$ values are not correlated with their U contents or Th/U ratios (Supplementary Data Tables S6 and S7).

The peralkaline granites show quintessential A-type chemical features (Collins *et al.*, 1982). While it has been suggested that peralkaline A-type granites have mafic precursors, their origin is enigmatic and may involve partial melting of crustal rocks or fractional crystallization of mantle-derived melts, and magma mixing between mantle-derived and crustal melts (Turner *et al.*, 1992; Kemp *et al.*, 2005; Scaillet & Macdonald, 2006; Yang *et al.*, 2006; Jahn *et al.*, 2009; Jeffery *et al.*, 2017; Jeffery & Gertisser, 2018). Low $\delta^{18}O$ values only occur in rocks that have been imprinted by hydrothermal interaction with meteoric water or seawater characterized by $\delta^{18}O < 0‰$ and *c.*0‰, respectively (Bindeman, 2011). Meteoric water could possibly be a source for the low zircon $\delta^{18}O$ values, given that the peralkaline granitoids crystallized in the shallow crust (see discussion above). However, the calc-alkaline granitoids were also emplaced in the shallow crust, but show mantle-like zircon $\delta^{18}O$ values that preclude the possibility of a meteoric water source. Furthermore, all zircons from the peralkaline granites have positive $\delta^{18}O$ values, which are inconsistent with a meteoric water contribution that would generate negative $\delta^{18}O$ values (Bindeman *et al.*, 2010). Thus, meteoric water plays a negligible role in the origin of these rocks. Therefore, the parental magmas of low $\delta^{18}O$ zircons are usually attributed to melting or assimilation of hydrothermally altered wall-rocks (Valley *et al.*, 2005; Pope *et al.*, 2013), re-melting of either preexisting low $\delta^{18}O$ high-temperature hydrothermally altered continental crust in shallow extensional environments or hydrothermally altered oceanic crust (Bindeman *et al.*, 2012; Boroughs *et al.*, 2012; Suzuki *et al.*, 2015; Dan *et al.*, 2019), or lithospheric mantle that has been modified by subducted high-temperature altered oceanic crust (Zhu *et al.*, 2017).

There are three possible candidates for the source of low $\delta^{18}O$ values in the Ulungur peralkaline granites of the East Junggar intra-oceanic arc: 1) Devonian volcanic-sedimentary rocks; 2) abnormal sub-arc mantle-derived sources; and 3) former oceanic crust that may possibly exist in the East Junggar mid-lower arc crust.

The Ulungur Pennsylvanian peralkaline granites intruded into the Devonian volcanic-sedimentary rocks. In addition, the peralkaline granites have variable whole rock Nd isotopic compositions with $\varepsilon_{Nd}(t)$ values ranging from +4·1 to +6·8 (Supplementary Data Table S8), indicating that crustal assimilation possibly plays an important role in their petrogenesis. No inherited zircons from the contaminants were found in peralkaline rocks, which may be due to the high temperature and alkali contents of the alkaline magma that prompts the dissolution of zircons (Watson, 1979). Although a role for crustal assimilation of the Devonian volcanic-sedimentary rocks in the origin of the peralkaline granites is possible, the relatively high $\delta^{18}O$ values in zircons (7·9–8·7‰) of the Devonian volcanic rocks intruded by the Ulungur granite plutons near Zhaheba (Liu & Liu, 2014), are inconsistent with an assimilation model for the peralkaline granites to account for their low zircon $\delta^{18}O$ values.

Previous studies have proposed that some alkaline rocks in NE China with low zircon $\delta^{18}O$ values were derived from fractional crystallization of mafic magmas derived from lithosphere mantle metasomatized by subducted high temperature altered oceanic crust (e.g. Zhu *et al.*, 2017). The Ulungur late Carboniferous peralkaline granites have Nd–Hf isotopic compositions similar to the Silurian to Devonian mafic rocks in the East Junggar, which were derived from a sub-arc mantle (Shen *et al.*, 2014), implying a possible common source. However, the Silurian to Devonian mafic rocks have low total alkaline contents ($Na_2O+K_2O = 4{\cdot}3$–$5{\cdot}7$ wt %) and are sodic with Na_2O/K_2O ratios of 1·4 to 4·9 (Shen *et al.*, 2014), distinct from those of the high K_2O late Carboniferous peralkaline granites. Thus, crystal fractionation of a sodic, mafic magma from sub-arc mantle is a virtually impossible petrogenetic scenario for the peralkaline granites. Furthermore, the $\delta^{18}O$ values in the local mantle are best reflected by the coeval gabbro and mafic dikes in the Ulungur region because they were generated by partial melting of sub-arc mantle. Zircons in the Ulungur gabbro examined in this study and nearby late Carboniferous Ertaibei mafic dyke, however, have $\delta^{18}O$ values ranging from mantle-like (5·3‰) to higher values (6·8‰) (Tang *et al.*, 2017*b*). This evidence argues against the sub-arc mantle as a source of the low $\delta^{18}O$ values and suggests the involvement of low $\delta^{18}O$ crustal sources for the peralkaline granites.

Intra-oceanic arcs are built upon oceanic crust (Sengör *et al.*, 1993; Suzuki *et al.*, 2015), and altered lower crust could be preserved beneath these features, as evidenced by geophysical data together with the xenoliths contained in lavas in modern intra-oceanic arcs (Price *et al.*, 2012). The Ulungur granites were formed in an intra-oceanic arc, which probably consisted of underthrust or trapped oceanic crust that served as the source of the peralkaline granites. Results from modern oceanic crust (Kempton *et al.*, 1991; Lécuyer & Gruau, 1996) and ophiolites (Gregory & Taylor, 1981; Muehlenbachs, 1986; Yamaoka *et al.*, 2012) reveal a systematic variation trend in oxygen isotope compositions with depth, with low $\delta^{18}O$ values (2–4‰) in the middle to lower parts because of high-temperature exchange with seawater. Low $\delta^{18}O$ values (3·9–5·6‰) in zircons were documented in oceanic plagiogranites associated with ophiolites (Grimes *et al.*, 2013). Accordingly, the Ulungur peralkaline granites could plausibly have originated from the East Junggar lower arc crust, including preexisting oceanic crustal material. Zircons of the Ulungur peralkaline granites plot in the field of oceanic crust on the U vs Yb diagram (Grimes *et al.*, 2007) (Supplementary Data Fig. S3), supporting this scenario. The strongly depleted Nd–Hf isotope compositions (Fig. 11a) also support this conclusion: the young two-stage zircon Hf model ages (392 ± 79 Ma, 1SD, $n = 59$) and whole rock Nd model ages (381 ± 22 Ma, 1SD, $n = 30$) are consistent with the 500 to 373 Ma ages of the widespread East Junggar ophiolites (Tang *et al.*, 2007; Liu *et al.*, 2016; Luo *et al.*, 2017; Shen *et al.*, 2018), which probably represent oceanic crustal relics (Fig. 1b). In addition, whole rock Sr–Nd isotope compositions of the peralkaline granites are consistent with those of East Junggar ophiolites (Fig. 11b). Furthermore, the preserved Junggar lower to middle crust is characterized by a high seismic P-wave velocity of 6·7–7·4 km/s (Zhang *et al.*, 2011), which is similar to the Vp of oceanic lower crust (6·9–7·0 km/s) (Christensen & Salisbury, 1975), also suggesting that the basement of the Junggar segment consists of oceanic crust. It should be noted that there have been no magmatic or tectonic events since the Carboniferous in the Ulungur area. Thus, the seismic P-wave velocity could plausibly approximate that of the Carboniferous lower to middle crust. Therefore, geophysical, whole rock Sr–Nd, and zircon trace element and HF–O isotope data for the Ulungur peralkaline granites are all consistent with them originating from preexisting oceanic crust in the lower crust of an intra-oceanic arc.

The altered oceanic crust protolith was likely eclogitic in composition. Eclogite-derived melts have intermediate compositions (Spandler *et al.*, 2007), and thus have distinctive major element characteristics compared to peridotite melts of mafic to ultramafic compositions (Dasgupta *et al.*, 2007). For the major elements, we compared the experimental melts of eclogitic protoliths to the peralkaline granitoids in Figs 12 and 13. Although the experimental melts do not closely resemble the peralkaline granitoids, some melts have high K_2O contents and are compositionally close to syenites. The differences between the eclogite melts and peralkaline granitoids may be caused by the composition and degree of melting of the source and the depth of melting. For the trace elements, the two syenitic samples show fractionated REE patterns with slightly negative Eu anomalies (Fig. 14a), suggesting that they were derived from arc lower crust under high pressure where garnet is stable, consistent with an eclogitic protolith for the peralkaline granitoids.

Clinopyroxene–amphibole compositions: tracers of peralkaline granite magma evolution

The various plutons of the peralkaline series are characterized by similar textures, mineralogy, geochemistry and isotope compositions, and define a linear trend with increasing SiO_2 content, indicating a common magma evolution related to crystallization (Figs 12–13). Whole rock, clinopyroxene and amphibole show strong Ba, Sr and Eu negative anomalies, also indicating that the associated magmas underwent extensive fractional crystallization prior to emplacement (Figs 6 and 14a and b). Negative Eu and Sr anomalies were probably produced by the fractionation of feldspar (Drake & Weill, 1975). In addition, the negative Pb anomalies of clinopyroxene and amphibole suggest early removal of alkali feldspar because Pb is compatible in that phase (Nash & Crecraft, 1985) (Fig. 6b,d). Weaker negative Eu,

Ba, Sr, P and Ti anomalies of the syenitic granites relative to the peralkaline granites indicate that the syenitic melt was less affected by alkali feldspar, apatite and Fe–Ti-oxide fractionation. Thus, the syenitic granites were probably derived from a slightly less evolved melt, but from the same parental magma (Fig. 14c-d).

Clinopyroxene and amphibole show analogous evolutionary trends in major and trace element chemistry (Figs 5–6 and 8), which reflect the evolution of the granitic melt. They show zoning patterns from core to rim, increasing in Na, Fe^{3+}, and Ti along with decreasing Ca and Al (Figs 5 and 8) and define a distinct increase in magma peralkalinity. Similar geochemical trends in clinopyroxene and amphibole have been documented in detail by many authors (e.g. Marks *et al.*, 2004; Piilonen *et al.*, 2013; Vilalva *et al.*, 2016; Siegel *et al.*, 2017) and the compositional evolution from sodic–calcic to sodic varieties with differentiation is attributed to increasing magma peralkalinity. The relative trace element abundances of clinopyroxene and amphibole seem to be mainly influenced by magma composition and crystal-chemical effects (Marks *et al.*, 2004). Clinopyroxene and amphibole show a continuous decrease in LREE contents from Ca-rich minerals to their Na-rich counterparts for the Ulungur peralkaline granites (Fig. 6); a typical feature in peralkaline rocks due to early removal of LREE-rich accessory minerals such as apatite. The REE patterns for clinopyroxene and amphibole are clearly bimodal with enrichment of HREEs. This feature is widely attributed to REEs being incorporated into two crystallographic sites with different optimal cation radii (Bottazzi *et al.*, 1999; Vilalva *et al.*, 2016; Siegel *et al.*, 2017), rather than according to lattice-site elastic-strain effects (Blundy & Wood, 1994). The LREEs are preferentially incorporated into eight-fold coordinated sites (M4 in amphibole, M1 in clinopyroxene), and the HREEs are compatible with the six-fold coordinated sites (M2 in amphibole, M1 in clinopyroxene) owing to their smaller ionic radius. Thus, the HREEs are preferentially incorporated in the crystal structure, which is supported by HREE (Yb and Lu) abundances of amphibole and clinopyroxene higher than those of whole rock (Fig. 6). The late-stage aegirine that mantles arfvedsonite, however, is most probably influenced by the composition of the residual peralkaline liquids, rather than crystal-chemical effects. The Nb and Ta contents in these late-stage aegirines are markedly higher than those recorded in arfvedsonite, consistent with the inference of a greater preference of pentavalent HFSEs for amphibole compared to the clinopyroxene structure (Marks *et al.*, 2004) (Fig. 6). The replacement of arfvedsonite by late-stage aegirine is typically related to hydrothermal alteration by a residual peralkaline (Na, F)-rich orthomagmatic liquid.

The HFSE and HREE contents in peralkaline granites systematically increase with increasing SiO_2 contents and are coupled with decreasing $(La/Lu)_N$, suggesting HFSE enrichment and REE fractionation are attributed to magma evolution. Clinopyroxene and amphibole are two major HFSE and REE-rich minerals. Therefore, where early HFSE and HREE-minerals saturation was inhibited owing to the low melting temperature of clinopyroxene and amphibole (Scaillet & Macdonald, 2001), the HFSE and HREE are enriched in residual peralkaline melts during early magma evolution.

Petrological model for the generation and emplacement of calc-alkaline and peralkaline series granitoids

Previous studies have demonstrated that arc-related magmatism ceased at *c.*300 Ma in the Junggar segment, and thus the subduction of Paleo-Junggar oceanic lithosphere terminated at this time (Tang *et al.*, 2012*b*; 2017*a*; 2017*b*). In addition, the Junggar pre-300 Ma rocks have distinctly lower zircon $\delta^{18}O$ values ranging from 3·3 to 7·2‰ with an average of 5·90‰, whereas the Early Permian (post-300 Ma) rocks reveal much higher zircon $\delta^{18}O$ values (8·2 to 10·3‰) (Tang *et al.*, 2019). The zircon O isotopes reflect a dramatic geodynamic change for the Junggar segment at *c.*300 Ma, which is consistent with the transition from arc to post-collision at that time. Furthermore, the occurrence of dolerite and diorite porphyry dykes and peralkaline granites in the Ulungur complex suggest magma generation related to an extensional setting. Thus, we propose an integrated petrogenetic model that closely links the *c.*320 Ma Ulungur intrusive complex with the rollback of subducted Paleo-Junggar ocean slab lithosphere in an intra-oceanic arc stage (Fig. 16).

In the subducted oceanic slab roll-back model, generation of the Ulungur intrusive complex initially involved a regional thermal anomaly triggered by asthenospheric mantle upwelling and the subsequent melting of the overlying hydrated mantle wedge and lower crust. The parental magma of the calc-alkaline series, represented by dolerite dykes, originated from partial melting of a hydrous sub-arc mantle wedge under garnet peridotite facies as indicated by their high $[Gd/Yb]_N$ ratios (Fig. 14a). These magmas experienced high pressure (*c.*700 MPa) crystallization of ultramafic cumulates during their transit through the lower crust, which accounts for their low Mg# (<0·52), and were subsequently emplaced in the upper crust as evidenced by the low Al_2O_3 content in amphibole rims. Hornblende gabbro represents the (Pl+Hb)-rich cumulate mush formed during differentiation of the calc-alkaline basaltic andesitic melt. The crystallization sequence and mineral chemistry suggest that the hornblende gabbros most likely crystallized from water-rich, mildly evolved, basaltic andesitic melts at low pressure (*c.*200 MPa), and that the melts reached water saturation to crystalize calcic plagioclase. On the basis of whole-rock geochemical modelling, the intermediate to felsic rocks (diorite porphyry dyke and monzogranite) can be

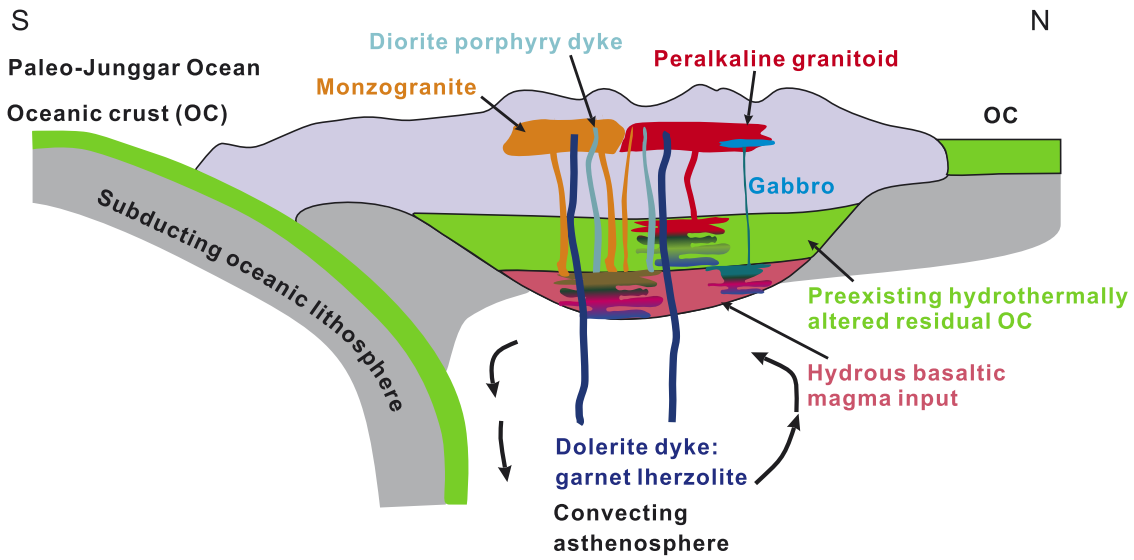

Fig. 16. Conceptual model of the stepwise incremental assembly and intra-crustal magmatic differentiation during the evolution of the Ulungur intrusive complex.

explained by upper crust fractional crystallization of dolerite dyke magmas, which was dominated by amphibole, plagioclase and minor biotite. In conclusion, the calc-alkaline magmatic series was generated from a depleted sub-arc mantle wedge source, following substantial crustal fractional crystallization. We note that although the rocks of the calc-alkaline series are closely linked in a magmatic evolutionary system, its various subgroups cannot be derived from a single parental magma based on the absolute age difference of 4 Ma (gabbro 314 Ma vs monzogranite 318–321 Ma) (Fig. 10b), and their distinct mineral geochemical variation trends (Fig. 4).

The peralkaline series originated from the melting of a preexisting oceanic crust in the lower crust of the Junggar intra-oceanic arc induced by asthenospheric mantle upwelling. The strongly depleted radiogenic Sr–Nd–Hf isotope compositions and low $\delta^{18}O$ (2·3–4·4‰) values of the peralkaline series are consistent with a magma source of hydrothermally altered gabbros at lower oceanic crustal levels. The magmas experienced fractional crystallization leading to the formation of a slightly less evolved magma (syenitic granite) and a more evolved magma (peralkaline granite). Early crystallization of clinopyroxene and amphibole was inhibited owing to their low melting temperature, leading to HFSE and HREE enrichment in the residual peralkaline melts during continuing crystallization.

Implications for crustal generation and reworking in accretionary orogens

The vast expanse of granitoids with depleted mantle-like Sr–Nd–Hf isotope compositions in the CAOB suggests a significant juvenile crust contribution. However, there is no consensus on their origin and models include derivation from the mantle (Jahn *et al.*, 2009), subducted oceanic crust (Tang *et al.*, 2010), juvenile arc crustal sources (Geng *et al.*, 2009; Tang *et al.*, 2012*b*) and residual oceanic crust (Tang *et al.*, 2012*a*; Liu *et al.*, 2013). These different models imply different modes of continental crust formation, and different rates of crustal generation. The calc-alkaline and peralkaline series granitoids of the Ulungur intrusive complex have different magma sources and the two series do not appear to show any interaction between the magmas during their ascent and differentiation. The two series preserve the chemical and isotopic characteristics of their parental magmas and represent two end-members of Junggar magmatism (Figs 12 and 13), and thus they provide an important clue to understanding crustal generation and reworking in accretionary orogens.

Extraction of juvenile material from the mantle for a sustained period, as represented by the Silurian–Carboniferous calc-alkaline series granitoids, represents generation of new crust, whereas melting of residual oceanic crust in the lower crust of the intra-oceanic arc for peralkaline granitoids corresponds to juvenile crust recycling linked to subduction of the Paleo-Junggar Ocean. Thus, we conclude that juvenile components in accretionary orogens can be derived from diverse magma sources, and that juvenile materials do not necessarily imply crust generation, but may also point to crustal reworking. Our results demonstrate that considerable amounts of juvenile material were derived from the reworking of previously generated residual oceanic crust, rather than from the mantle, and that crustal reworking plays an important role in continental crust formation for accretionary orogens. If our interpretation accurately describes the sources for peralkaline granitoids as derived from residual oceanic crust, then the rate of generation of new crust for the CAOB needs to be reevaluated.

CONCLUSIONS

The Ulungur intrusive complex includes calc-alkaline and peralkaline series granitoids. The two series show different chemical and isotopic characteristics that reflect distinct magma sources, depths of magma extraction and crystallization processes. They represent two endmembers of the Junggar magmatic rocks. Thus, the Ulungur intrusive complex provides new perspectives on CAOB magma sources and crystallization processes, and on crustal generation and reworking in the CAOB. The main conclusions that can be drawn from this study are:

1. Both the calc-alkaline and peralkaline series granitoids of the Ulungur intrusive complex have depleted mantle-like radiogenic Sr–Nd–Hf isotopic compositions. However, they have different zircon $\delta^{18}O$ values, indicating they were derived from different juvenile magma sources.
2. The calc-alkaline series granitoids are derived from a sub-arc mantle wedge based on their isotope compositions. On the basis of combining detailed petrography, mineral chemistry, and experimental mineral stability P–T diagrams with mineral thermobarometric calculations, we suggest that the mineral assemblage reflects differentiation in both the deep and shallow crust.
3. The peralkaline series granitoids are characterized by relatively low $\delta^{18}O$ (2·3–4·4‰) values and enrichment of HFSE and HREE. They originated from the melting of a preexisting residual oceanic crust in the lower crust of the Junggar intra-oceanic arc. Early crystallization of clinopyroxene and amphibole was inhibited owing to their low melting temperature, leading to HFSE and HREE enrichment in residual peralkaline melts during continuing crystallization.
4. The calc-alkaline and peralkaline series granitoids represent crust generation and reworking, respectively, indicating that the juvenile components in accretionary orogens can be derived from diverse magma sources (sub-arc mantle wedge or residual oceanic crust). Crust reworking plays an important role in continental crust formation, and the rate of crust formation needs to be reevaluated for the CAOB.

ACKNOWLEDGMENTS

Le Zhang, Qing Yang and Xiao-Ping Xia are thanked for help with the LA-ICPMS and the SIMS analyses. We thank Georg Zellmer for editorial handling, and Min Sun, Emily J. Chin and Kwan-Nang Pang for their constructive and helpful reviews on the manuscript.

FUNDING

This study was supported by the National Key R & D Program of China (2017YFC0601205), the Strategic Priority Research Program (B) of the Chinese Academy of Sciences (grant XDB18020204), the National Natural Science Foundation of China (grants 41722205, 41673033, 41630208 and U1703125), the Key Program of the Chinese Academy of Sciences (QYZDJ-SSW-DQC026), the Youth Innovation Promotion Association, CAS (Y201966), and the Second Tibetan Plateau Scientific Expedition and Research Program (STEP) (2019QZKK0702). This is contribution 2813 from GIG-CAS.

SUPPLEMENTARY DATA

Supplementary data are available at *Journal of Petrology* online.

REFERENCES

Acosta-Vigil, A., Buick, I., Hermann, J., Cesare, B., Rubatto, D., London, D. & Morgan, G. B. VI. (2010). Mechanisms of crustal anatexis: a geochemical study of partially melted metapelitic enclaves and host dacite, SE Spain. *Journal of Petrology* **51**, 785–821.

Anderson, J. L., Barth, A. P., Wooden, J. L. & Mazdab, F. (2008). Thermometers and thermobarometers in granitic systems. *Reviews in Mineralogy and Geochemistry* **69**, 121–142.

Andujar, J., Scaillet, B., Pichavant, M. & Druitt, T. H. (2015). Differentiation conditions of a Basaltic Magma from Santorini, and its bearing on the production of andesite in arc settings. *Journal of Petrology* **56**, 765–794.

Andujar, J., Scaillet, B., Pichavant, M. & Druitt, T. H. (2016). Generation conditions of dacite and rhyodacite via the crystallization of an andesitic magma. Implications for the plumbing system at santorini (Greece) and the origin of tholeiitic or calc-alkaline differentiation trends in arc magmas. *Journal of Petrology* **57**, 1887–1920.

Barnes, C. G., Memeti, V. & Coint, N. (2016). Deciphering magmatic processes in calc-alkaline plutons using trace element zoning in hornblende. *American Mineralogist* **101**, 328–342.

Bindeman, I. (2011). When do we need pan-global freeze to explain 18O-depleted zircons and rocks? *Geology* **39**, 799–800.

Bindeman, I., Gurenko, A., Carley, T., Miller, C., Martin, E. & Sigmarsson, O. (2012). Silicic magma petrogenesis in Iceland by remelting of hydrothermally altered crust based on oxygen isotope diversity and disequilibria between zircon and magma with implications for MORB. *Terra Nova* **24**, 227–232.

Bindeman, I. N., Schmitt, A. K. & Evans, D. A. D. (2010). Limits of hydrosphere-lithosphere interaction: origin of the lowest-known δ18O silicate rock on Earth in the Paleoproterozoic Karelian rift. *Geology* **38**, 631–634.

Blatter, D. L., Sisson, T. W. & Hankins, W. B. (2013). Crystallization of oxidized, moderately hydrous arc basalt at mid- to lower-crustal pressures: implications for andesite genesis. *Contributions to Mineralogy and Petrology* **166**, 861–886.

Blundy, J. & Wood, B. (1994). Prediction of crystal–melt partition coefficients from elastic moduli. *Nature* **372**, 452–454.

Boroughs, S., Wolff, J. A., Ellis, B. S., Bonnichsen, B. & Larson, P. B. (2012). Evaluation of models for the origin of Miocene low-δ18O rhyolites of the Yellowstone/Columbia River Large Igneous Province. *Earth and Planetary Science Letters* **313–314**, 45–55.

Bottazzi, P., Tiepolo, M., Vannucci, R., Zanetti, A., Brumm, R., Foley, S. F. & Oberti, R. (1999). Distinct site preferences for heavy and light REE in amphibole and the prediction of

Amph/LDREE. *Contributions to Mineralogy and Petrology* **137**, 36–45.

Bucholz, C. E., Jagoutz, O., Schmidt, M. W. & Sambuu, O. (2014). Fractional crystallization of high-K arc magmas: biotite- versus amphibole-dominated fractionation series in the Dariv Igneous Complex, Western Mongolia. *Contributions to Mineralogy and Petrology* **168**, 1072–1100.

Cawood, P. A., Hawkesworth, C. J. & Dhuime, B. (2013). The continental record and the generation of continental crust. *Geological Society of America Bulletin* **125**, 14–32.

Cawood, P. A., Kroner, A., Collins, W. J., Kusky, T. M., Mooney, W. D. & Windley, B. F. (2009). Accretionary orogens through Earth history. *Geological Society of London*, **318**, 1–36.

Chen, B. & Arakawa, Y. (2005). Elemental and Nd-Sr isotopic geochemistry of granitoids from the West Junggar foldbelt (NW China), with implications for Phanerozoic continental growth. *Geochimica et Cosmochimica Acta* **69**, 1307–1320.

Chen, J. F., Han, B. F., Ji, J. Q., Zhang, L., Xu, Z., He, G. Q. & Wang, T. (2010). Zircon U–Pb ages and tectonic implications of Paleozoic plutons in northern West Junggar, North Xinjiang, China. *Lithos* **115**, 137–152.

Chen, B. & Jahn, B. M. (2004). Genesis of post-collisional granitoids and basement nature of the Junggar Terrane, NW China: Nd-Sr isotope and trace element evidence. *Journal of Asian Earth Sciences* **23**, 691–703.

Chin, E. J., Lee, C. T. A. & Barnes, J. D. (2014). Thickening, refertilization, and the deep lithosphere filter in continental arcs: constraints from major and trace elements and oxygen isotopes. *Earth and Planetary Science Letters* **397**, 184–200.

Christensen, N. I. & Salisbury, M. H. (1975). Structure and constitution of the lower oceanic crust. *Reviews of Geophysics* **13**, 57–86.

Collins, W., Beams, S., White, A. & Chappell, B. (1982). Nature and origin of A-type granites with particular reference to southeastern Australia. *Contributions to Mineralogy and Petrology* **80**, 189–200.

Dan, W., Wang, Q., Li, X.-H., Tang, G.-J., Zhang, C., Zhang, X.-Z. & Wang, J. (2019). Low δ18O magmas in the carboniferous intra-oceanic arc, central Tibet: implications for felsic magma generation and oceanic arc accretion. *Lithos* **326-327**, 28–38.

Dasgupta, R., Hirschmann, M. & Smith, N. (2007). Partial melting experiments of peridotite + CO2 at 3 GPa and Genesis of Alkalic Ocean Island Basalts. *Journal of Petrology* **48**, 2093–2124.

Davidson, J. P. & Arculus, R. J. (2006). The significance of phanerozoic arc magmatism in generating continental crust. In: Brown, M., and Rushmer, T. (eds) *Evolution and Differentiation of the Continental Crust*. Cambridge, UK: Cambridge University Press, pp. 135–172.

Davidson, J., Turner, S., Handley, H., Macpherson, C. & Dosseto, A. (2007). Amphibole "sponge" in arc crust? *Geology* **35**, 787–790.

Drake, M. J. & Weill, D. F. (1975). Partition of Sr, Ba, Ca, Y, Eu2+, Eu3+, and other REE between plagioclase feldspar and magmatic liquid: an experimental study. *Geochimica et Cosmochimica Acta* **39**, 689–712.

Ferry, J. & Watson, E. (2007). New thermodynamic models and revised calibrations for the Ti-in-zircon and Zr-in-rutile thermometers. *Contributions to Mineralogy and Petrology* **154**, 429–437.

Gao, Y. Y., Li, X. H., Griffin, W. L., O'Reilly, S. Y. & Wang, Y. F. (2014). Screening criteria for reliable U–Pb geochronology and oxygen isotope analysis in uranium-rich zircons: a case study from the Suzhou A-type granites, SE China. *Lithos* **192–195**, 180–191.

Geng, H., Sun, M., Yuan, C., Xiao, W., Xian, W., Zhao, G., Zhang, L., Wong, K. & Wu, F. (2009). Geochemical, Sr–Nd and zircon U–Pb-Hf isotopic studies of Late Carboniferous magmatism in the West Junggar, Xinjiang: implications for ridge subduction? *Chemical Geology* **266**, 364–389.

Geng, H., Sun, M., Yuan, C., Zhao, G. & Xiao, W. (2011). Geochemical and geochronological study of early Carboniferous volcanic rocks from the West Junggar: petrogeneses and tectonic implications. *Journal of Asian Earth Sciences* **42**, 854–866.

Gori, C., Tribaudino, M., Mantovani, L., Delmonte, D., Mezzadri, F., Gilioli, E. & Calestani, G. (2015). Ca-Zn solid solutions in C2/c pyroxenes: synthesis, crystal structure, and implications for Zn geochemistry. *American Mineralogist* **100**, 2209–2218.

Gregory, R. T. & Taylor, H. P. (1981). An oxygen isotope profile in a section of Cretaceous oceanic crust, Samail Ophiolite, Oman: evidence for δ18O buffering of the oceans by deep (>5 km) seawater-hydrothermal circulation at mid-ocean ridges. *Journal of Geophysical Research: Solid Earth* **86**, 2737–2755.

Griffin, W. L., Pearson, N. J., Belousova, E. A. & Saeed, A. (2006). Comment: Hf-isotope heterogeneity in zircon 91500. *Chemical Geology* **233**, 358–363.

Grimes, C. B., John, B. E., Kelemen, P. B., Mazdab, F. K., Wooden, J. L., Cheadle, M. J., Hanghoj, K. & Schwartz, J. J. (2007). Trace element chemistry of zircons from oceanic crust: a method for distinguishing detrital zircon provenance. *Geology* **35**, 643–646.

Grimes, C. B., Ushikubo, T., Kozdon, R. & Valley, J. W. (2013). Perspectives on the origin of plagiogranite in ophiolites from oxygen isotopes in zircon. *Lithos* **179**, 48–66.

Grove, T. L., Elkins-Tanton, L. T., Parman, S. W., Chatterjee, N., Müntener, O. & Gaetani, G. A. (2003). Fractional crystallization and mantle-melting controls on calc-alkaline differentiation trends. *Contributions to Mineralogy and Petrology* **145**, 515–533.

Han, B. F., Wang, S. G., Jahn, B. M., Hong, D. W., Kagami, H. & Sun, Y. L. (1997). Depleted-mantle source for the Ulungur River A-type granites from North Xinjiang, China: geochemistry and Nd-Sr isotopic evidence, and implications for Phanerozoic crustal growth. *Chemical Geology* **138**, 135–159.

Hargrove, U. S., Stern, R. J., Kimura, J. I., Manton, W. I. & Johnson, P. R. (2006). How juvenile is the Arabian–Nubian Shield? Evidence from Nd isotopes and pre-Neoproterozoic inherited zircon in the Bi'r Umq suture zone, Saudi Arabia. *Earth and Planetary Science Letters* **252**, 308–326.

Hawthorne, F. C., Oberti, R., Harlow, G. E., Maresch, W. V., Martin, R. F., Schumacher, J. C. & Welch, M. D. (2012). Nomenclature of the amphibole supergroup. *American Mineralogist* **97**, 2031–2048.

Jackson, S. E., Pearson, N. J., Griffin, W. L. & Belousova, E. A. (2004). The application of laser ablation-inductively coupled plasma-mass spectrometry to in situ U–Pb zircon geochronology. *Chemical Geology* **211**, 47–69.

Jahn, B. M. (2004). The Central Asian Orogenic Belt and Growth of the Continental Crust in the Phanerozoic. In: Malpas, J., Fletcher, C. J. N., Ali, J. R. and Aichison, J. C. (eds.) *Aspects of the Tectonic Evolution of China*. London: Geological Society, London, Special Publications, 73–100.

Jahn, B. M., Litvinovsky, B. A., Zanvilevich, A. N. & Reichow, M. (2009). Peralkaline granitoid magmatism in the Mongolian-Transbaikalian Belt: evolution, petrogenesis and tectonic significance. *Lithos* **113**, 521–539.

Jahn, B. M., Wu, F. Y. & Chen, B. (2000). Massive granitoid generation in Central Asia: Ndisotope evidence and implication

for continental growth in the Phanerozoic. *Episodes* **23**, 82–92.

Jeffery, A. J. & Gertisser, R. (2018). Peralkaline felsic magmatism of the Atlantic Islands. *Frontiers in Earth Science* **6,** 145.

Jeffery, A. J., Gertisser, R., Self, S., Pimentel, A., O'Driscoll, B. & Pacheco, J. M. (2017). Petrogenesis of the Peralkaline Ignimbrites of Terceira, Azores. *Journal of Petrology* **58**, 2365–2401.

Kay, R. W., Rubenstone, J. L. & Kay, S. M. (1986). Aleutian terranes from Nd isotopes. *Nature* **322**, 605–609.

Kemp, A. I. S., Hawkesworth, C. J., Collins, W. J., Gray, C. M. & Blevin, P. L. (2009). Isotopic evidence for rapid continental growth in an extensional accretionary orogen: the Tasmanides, eastern Australia. *Earth and Planetary Science Letters* **284**, 455–466.

Kemp, A. I. S., Wormald, R. J., Whitehouse, M. J. & Price, R. C. (2005). Hf isotopes in zircon reveal contrasting sources and crystallization histories for alkaline to peralkaline granites of Temora, southeastern Australia. *Geology* **33**, 797–800.

Kempton, P. D., Hawkesworth, C. J. & Fowler, M. B. (1991). Geochemistry and isotopic composition of gabbros from-layer 3 of the Indian Ocean crust, Hole 735B. In: Von Herzen, R.P.Robinson, P. T. (eds) *Proceedings of the Ocean Drilling Program-Scientific Results, 118,* College Station, TX: Ocean Drilling Program, pp. 127–141.

Khain, E. V., Bibikova, E. V., Kroner, A., Zhuravlev, D. Z., Sklyarov, E. V., Fedotova, A. A. & Kravchenko-Berezhnoy, I. R. (2002). The most ancient ophiolite of the Central Asian fold belt: U–Pb and Pb-Pb zircon ages for the Dunzhugur Complex, Eastern Sayan, Siberia, and geodynamic implications. *Earth and Planetary Science Letters* **199**, 311–325.

Klaver, M., Matveev, S., Berndt, J., Lissenberg, C. J. & Vroon, P. Z. (2017). A mineral and cumulate perspective to magma differentiation at Nisyros volcano, Aegean arc. *Contributions to Mineralogy and Petrology* **172**, 1–23.

Krawczynski, M. J., Grove, T. L. & Behrens, H. (2012). Amphibole stability in primitive arc magmas: effects of temperature, H2O content, and oxygen fugacity. *Contributions to Mineralogy and Petrology* **164**, 317–339.

Kröner, A., Kovach, V., Alexeiev, D., Wang, K. L., Wong, J., Degtyarev, K. & Kozakov, I. (2017). No excessive crustal growth in the Central Asian Orogenic Belt: further evidence from field relationships and isotopic data. *Gondwana Research* **50**, 135–166.

Kröner, A., Kovach, V., Belousova, E., Hegner, E., Armstrong, R., Dolgopolova, A., Seltmann, R., Alexeiev, D. V., Hoffmann, J. E., Wong, J., Sun, M., Cai, K., Wang, T., Tong, Y., Wilde, S. A., Degtyarev, K. E. & Rytsk, E. (2014). Reassessment of continental growth during the accretionary history of the Central Asian Orogenic Belt. *Gondwana Research* **25**, 103–125.

Kröner, A., Windley, B. F., Badarch, G., Tomurtogoo, O., Hegner, E., Jahn, B. M., Gruschka, S., Khain, E. V., Demoux, A. & Wingate, M. T. D. (2007). Accretionary Growth and Crust Formation in the Central Asian Orogenic Belt and Comparison with the Arabian-Nubian Shield. In: Hatcher, R. D.Jr, Carlson, M. P., and McBride, J. H. (eds) *A 4-D Framework of Continental Crust*: Boulder, Colorado, Geological Society of America Memoirs, 200, pp. 181–209.

Le Maitre, R. W. (2002). *Igneous Rocks: A Classification and Glossary of Terms: Recommendations of the International Union of Geological Sciences Subcommission on the Systematics of Igneous Rocks*. Cambridge: Cambridge University Press, 236 pp.

Lécuyer, C. & Gruau, G. (1996). Oxygen and strontium isotope compositions of Hess Deep gabbros (Holes 894F and 894G): high-temperature interaction of seawater with the oceanic crust layer 3. In: Mével, C., Gillis, K. M., Allan, J. F.Meyer, P. S. (eds) *Proceedings of the Ocean Drilling Program-Scientific Results* 147, College Station, TX: Ocean Drilling Program, pp. 227–234.

Li, D., He, D. F., Santosh, M. & Tang, J. Y. (2014). Petrogenesis of Late Paleozoic volcanics from the Zhaheba depression, East Junggar: insights into collisional event in an accretionary orogen of Central Asia. *Lithos* **184–187**, 167–193.

Li, Q. L., Li, X. H., Liu, Y., Tang, G. Q., Yang, J. H. & Zhu, W. G. (2010). Precise U–Pb and Pb-Pb dating of Phanerozoic baddeleyite by SIMS with oxygen flooding technique. *Journal of Analytical Atomic Spectrometry* **25**, 1107–1113.

Li, X. H., Li, Z. X., Sinclair, J. A., Li, W. X. & Carter, G. (2006). Revisiting the "Yanbian Terrane": implications for Neoproterozoic tectonic evolution of the western Yangtze Block, South China. *Precambrian Research* **151**, 14–30.

Li, X. H., Liu, Y., Li, Q. L., Guo, C. H. & Chamberlain, K. R. (2009). Precise determination of Phanerozoic zircon Pb/Pb age by multicollector SIMS without external standardization. *Geochemistry, Geophysics, Geosystems* **10**, Q04010.

Li, X. H., Long, W. G., Li, Q. L., Liu, Y., Zheng, Y. F., Yang, Y. H., Chamberlain, K. R., Wan, D. F., Guo, C. H., Wang, X. C. & Tao, H. (2010). Penglai Zircon Megacrysts: a potential new working reference material for microbeam determination of HF–O Isotopes and U–Pb Age. *Geostandards and Geoanalytical Research* **34**, 117–134.

Li, X. H., Tang, G. Q., Gong, B., Yang, Y. H., Hou, K. J., Hu, Z. C., Li, Q. L., Liu, Y. & Li, W. X. (2013). Qinghu zircon: a working reference for microbeam analysis of U–Pb age and Hf and O isotopes. *Chinese Science Bulletin* **58**, 4647–4654.

Liu, W., Liu, X. J. & Liu, L. Y. (2013). Underplating generated A- and I-type granitoids of the East Junggar from the lower and the upper oceanic crust with mixing of mafic magma: insights from integrated zircon U–Pb ages, petrography, geochemistry and Nd–Sr–Hf isotopes. *Lithos* **179**, 293–319.

Liu, X. & Liu, W. (2014). Source characteristics and tectonic setting of the Early and Middle Devonian volcanic rocks in the North Junggar, Northwest China: insights from Nd–Sr isotopes and geochemistry. *Lithos* **184–187**, 27–41.

Liu, X., Xiao, W., Xu, J., Castillo, P. R. & Shi, Y. (2017). Geochemical signature and rock associations of ocean ridge-subduction: evidence from the Karamaili Paleo-Asian ophiolite in east Junggar, NW China. *Gondwana Research* **48**, 34–49.

Liu, Y. R., Jian, P., Zhang, W., Shi, Y. R., Wang, Y. Z., Zhang, L. Q. & Liu, D. Y. (2016). Zircon SHRIMP U–Pb dating and O isotope of the Beitashan ophiolitic mélange in the East Junggar, Xinjiang, and its geological significance. *Acta Petrologica Sinica* **32**, 537–554.

Locock, A. J. (2014). An Excel spreadsheet to classify chemical analyses of amphiboles following the IMA 2012 recommendations. *ComputersGeosciences* **62**, 1–11.

Ludwig, K. R. (2003). User's manual for Isoplot 3.00: a geochronological toolkit for Microsoft Excel. *Berkeley Geochronology Center Special Publication* **4**, 1–70.

Luo, J., Xiao, W., Wakabayashi, J., Han, C., Zhang, J. e., Wan, B., Ao, S., Zhang, Z., Tian, Z., Song, D. & Chen, Y. (2017). The Zhaheba ophiolite complex in Eastern Junggar (NW China): long lived supra-subduction zone ocean crust formation and its implications for the tectonic evolution in southern Altaids. *Gondwana Research* **43**, 17–40.

Maniar, P. D. & Piccoli, P. M. (1989). Tectonic discrimination of granitoids. *Geological Society of America Bulletin* **101**, 635–643.

Marks, M., Halama, R., Wenzel, T. & Markl, G. (2004). Trace element variations in clinopyroxene and amphibole from alkaline to peralkaline syenites and granites: implications for

mineral-melt trace-element partitioning. *Chemical Geology* **211**, 185–215.

Melekhova, E., Blundy, J., Robertson, R. & Humphreys, M. C. S. (2015). Experimental evidence for polybaric differentiation of primitive arc basalt beneath St. Vincent, Lesser Antilles. *Journal of Petrology* **56**, 161–192.

Moore, G. & Carmichael, I. S. E. (1998). The hydrous phase equilibria (to 3 kbar) of an andesite and basaltic andesite from western Mexico: constraints on water content and conditions of phenocryst growth. *Contributions to Mineralogy and Petrology* **130**, 304–319.

Muehlenbachs, K. (1986). Alteration of the oceanic crust and the 18O history of seawater. *Reviews in Mineralogy and Geochemistry* **16**, 425–444.

Müntener, O., Ewing, T., Baumgartner, L. P., Manzini, M., Roux, T., Pellaud, P. & Allemann, L. (2018). Source and fractionation controls on subduction-related plutons and dike swarms in southern Patagonia (Torres del Paine area) and the low Nb/Ta of upper crustal igneous rocks. *Contributions to Mineralogy and Petrology* **173**, 38.

Müntener, O., Kelemen, P. & Grove, T. (2001). The role of H2O during crystallization of primitive arc magmas under uppermost mantle conditions and genesis of igneous pyroxenites: an experimental study. *Contributions to Mineralogy and Petrology* **141**, 643–658.

Mutch, E. J. F., Blundy, J. D., Tattitch, B. C., Cooper, F. J. & Brooker, R. A. (2016). An experimental study of amphibole stability in low-pressure granitic magmas and a revised Al-in-hornblende geobarometer. *Contributions to Mineralogy and Petrology* **171**, 85.

Nandedkar, R. H., Hürlimann, N., Ulmer, P. & Müntener, O. (2016). Amphibole–melt trace element partitioning of fractionating calc-alkaline magmas in the lower crust: an experimental study. *Contributions to Mineralogy and Petrology* **171**, 71.

Nandedkar, R., Ulmer, P. & Müntener, O. (2014). Fractional crystallization of primitive, hydrous arc magmas: an experimental study at 0.7 GPa. *Contributions to Mineralogy and Petrology* **167**, 1–27.

Nash, W. P. & Crecraft, H. R. (1985). Partition coefficients for trace elements in silicic magmas. *Geochimica et Cosmochimica Acta* **49**, 2309–2322.

Peccerillo, A. & Taylor, S. R. (1976). Geochemistry of Eocene calc-alkaline volcanic rocks from the Kastamonu area, Northern Turkey. *Contributions to Mineralogy and Petrology* **58**, 63–81.

Pichavant, M. & Macdonald, R. (2007). Crystallization of primitive basaltic magmas at crustal pressures and genesis of the calc-alkaline igneous suite: experimental evidence from St Vincent, Lesser Antilles arc. *Contributions to Mineralogy and Petrology* **154**, 535–558.

Pichavant, M., Martel, C., Bourdier, J.-L. & Scaillet, B. (2002). Physical conditions, structure, and dynamics of a zoned magma chamber: Mount Pelée (Martinique, Lesser Antilles Arc). *Journal of Geophysical Research* **107,** 2093.

Piilonen, P. C., McDonald, A. M., Poirier, G., Rowe, R. & Larsen, A. O. (2013). Mafic minerals of the alkaline pegmatites in the Larvik plutonic complex, Oslo Rift, Southern Norway. *The Canadian Mineralogist* **51**, 735–770.

Pope, E. C., Bird, D. K. & Arnórsson, S. (2013). Evolution of low-18O Icelandic crust. *Earth and Planetary Science Letters* **374**, 47–59.

Price, R. C., Gamble, J. A., Smith, I. E. M., Maas, R., Waight, T., Stewart, R. B. & Woodhead, J. (2012). The anatomy of an Andesite Volcano: a time-stratigraphic study of andesite petrogenesis and crustal evolution at Ruapehu Volcano, New Zealand. *Journal of Petrology* **53**, 2139–2189.

Ren, R., Han, B. F., Xu, Z., Zhou, Y. Z., Liu, B., Zhang, L., Chen, J. F., Su, L., Li, J., Li, X. H. & Li, Q. L. (2014). When did the subduction first initiate in the southern Paleo-Asian Ocean: new constraints from a Cambrian intra-oceanic arc system in West Junggar, NW China. *Earth and Planetary Science Letters* **388**, 222–236.

Righter, K. & Carmichael, I. S. E. (1996). Phase equilibria of phlogopite lamprophyres from western Mexico: biotite-liquid equilibria and P-T estimates for biotite-bearing igneous rocks. *Contributions to Mineralogy and Petrology* **123**, 1–21.

Rutherford, M. J. & Devine, J. D. (2003). Magmatic conditions and magma ascent as indicated by hornblende phase equilibria and reactions in the 1995-2002 Soufriere Hills magma. *Journal of Petrology* **44**, 1433–1454.

Samson, S. D., McClelland, W. C., Patchett, P. J., Gehrels, G. E. & Anderson, R. G. (1989). Evidence from neodymium isotopes for mantle contributions to Phanerozoic crustal genesis in the Canadian Cordillera. *Nature* **337**, 705–709.

Scaillet, B. & Macdonald, R. (2001). Phase relations of peralkaline silicic magmas and petrogenetic implications. *Journal of Petrology* **42**, 825–845.

Scaillet, B. & Macdonald, R. (2006). Experimental constraints on pre-eruption conditions of pantelleritic magmas: evidence from the Eburru complex, Kenya Rift. *Lithos* **91**, 95–108.

Scaillet, B., Holtz, F. & Pichavant, M. (2016). Experimental constraints on the formation of silicic magmas. *Elements* **12**, 109–114.

Sengör, A. M. C., Natal'in, B. A. & Burtman, V. S. (1993). Evolution of the Altaid tectonic collage and Palaeozoic crustal growth in Eurasia. *Nature* **364**, 299–307.

Shand, S. J. (1943). *Eruptive Rocks: their Genesis. Composition, Classification, and Their Relations to Ore-Deposits*. New York: John Wiley, 444 pp.

Shaw, D. M. (2000). Continuous (dynamic) melting theory revisited. *The Canadian Mineralogist* **38**, 1041–1063.

Shen, P., Shen, Y., Li, X.-H., Pan, H., Zhu, H., Meng, L. & Dai, H. (2012). Northwestern Junggar Basin, Xiemisitai Mountains, China: a geochemical and geochronological approach. *Lithos* **140–141**, 103–118.

Shen, X., Zhang, H., Wang, Q., Wyman, D. A. & Yang, Y. (2011). Late Devonian–Early Permian A-type granites in the southern Altay Range, Northwest China: petrogenesis and implications for tectonic setting of "A2-type" granites. *Journal of Asian Earth Sciences* **42**, 986–1007.

Shen, X.-M., Zhang, H.-X., Wang, Q., Ma, L. & Yang, Y.-H. (2014). Early Silurian (~440Ma) adakitic, andesitic and Nb-enriched basaltic lavas in the southern Altay Range, Northern Xinjiang (western China): slab melting and implications for crustal growth in the Central Asian Orogenic Belt. *Lithos* **206–207**, 234–251.

Shen, X.-M., Zhang, H.-X., Wang, Q., Saha, A. & Ma, L. (2018). Zircon U–Pb geochronology and geochemistry of Devonian plagiogranites in the Kuerti area of southern Chinese Altay, northwest China: petrogenesis and tectonic evolution of late Paleozoic ophiolites. *Geological Journal* **53**, 1886–1905.

Siegel, K., Williams-Jones, A. E. & van Hinsberg, V. J. (2017). The amphiboles of the REE-rich A-type peralkaline Strange Lake pluton—fingerprints of magma evolution. *Lithos* **288-289**, 156–174.

Sisson, T. W. & Grove, T. L. (1993). Experimental investigations of the role of H2O in calc-alkaline differentiation and subduction zone magmatism. *Contributions to Mineralogy and Petrology* **113**, 143–166.

Sláma, J., Košler, J., Condon, D. J., Crowley, J. L., Gerdes, A., Hanchar, J. M., Horstwood, M. S. A., Morris, G. A., Nasdala, L., Norberg, N., Schaltegger, U., Schoene, B., Tubrett, M. N.

& Whitehouse, M. J. (2008). Plešovice zircon—a new natural reference material for U–Pb and Hf isotopic microanalysis. *Chemical Geology* **249**, 1–35.

Smith, D. J. (2014). Clinopyroxene precursors to amphibole sponge in arc crust. *Nature Communications* **5**, 4329.

Spandler, C., Yaxley, G., Green, D. & Rosenthal, A. (2007). Phase relations and melting of anhydrous k-bearing eclogite from 1200 to 1600 C and 3 to 5 GPa. *Journal of Petrology* **49**, 771–795.

Streckeisen, A. (1974). Classification and nomenclature of plutonic rocks recommendations of the IUGS subcommission on the systematics of Igneous Rocks. *Geologische Rundschau* **63**, 773–786.

Su, Y., Zheng, J., Griffin, W. L., Zhao, J., Tang, H., Ma, Q. & Lin, X. (2012). Geochemistry and geochronology of Carboniferous volcanic rocks in the eastern Junggar terrane, NW China: implication for a tectonic transition. *Gondwana Research* **22**, 1009–1029.

Sun, S. S. & McDonough, W. F. (1989). Chemical and isotopic systematics of oceanic basalts: implications for mantle composition and processes. In: Saunders, A. D. and Norry, M. J. (eds.) *Magmatism in the Ocean Basins. London: Geological Society,* London, Special Publications, 42, pp. 313–345.

Suzuki, K., Kitajima, K., Sawaki, Y., Hattori, K., Hirata, T. & Maruyama, S. (2015). Ancient oceanic crust in island arc lower crust: evidence from oxygen isotopes in zircons from the Tanzawa Tonalitic Pluton. *Lithos* **228–229**, 43–54.

Takagi, D., Sato, H. & Nakagawa, M. (2005). Experimental study of a low-alkali tholeiite at 1-5 kbar: optimal condition for the crystallization of high—an plagioclase in hydrous arc tholeiite. *Contributions to Mineralogy and Petrology* **149**, 527–540.

Tang, G.-J., Chung, S.-L., Hawkesworth, C. J., Cawood, P. A., Wang, Q., Wyman, D. A., Xu, Y.-G. & Zhao, Z.-H. (2017a). Short episodes of crust generation during protracted accretionary processes: evidence from Central Asian Orogenic Belt, NW China. *Earth and Planetary Science Letters* **464**, 142–154.

Tang, G.-J., Wang, Q., Wyman, D. A. & Dan, W. (2019). Crustal maturation through chemical weathering and crustal recycling revealed by Hf–O–B isotopes. *Earth and Planetary Science Letters* **524**, 115709.

Tang, G. J., Wang, Q., Wyman, D. A., Li, Z. X., Xu, Y. G. & Zhao, Z. H. (2012a). Recycling oceanic crust for continental crustal growth: Sr–Nd–Hf isotope evidence from granitoids in the western Junggar region, NW China. *Lithos* **128-131**, 73–83.

Tang, G. J., Wang, Q., Wyman, D. A., Li, Z. X., Zhao, Z. H., Jia, X. H. & Jiang, Z. Q. (2010). Ridge subduction and crustal growth in the Central Asian Orogenic Belt: evidence from Late Carboniferous adakites and high-Mg diorites in the western Junggar region, northern Xinjiang (west China). *Chemical Geology* **227**, 281–300.

Tang, G. J., Wang, Q., Wyman, D. A., Li, Z. X., Zhao, Z. H. & Yang, Y. H. (2012b). Late Carboniferous high εNd(t)–εHf(t) granitoids, enclaves and dikes in western Junggar, NW China: ridge-subduction-related magmatism and crustal growth. *Lithos* **140–141**, 86–102.

Tang, G.-J., Wang, Q., Zhang, C., Wyman, D. A., Dan, W., Xia, X.-P., Chen, H.-Y. & Zhao, Z.-H. (2017b). Sr–Nd-HF–O isotope geochemistry of the Ertaibei pluton, East Junggar, NWChina: implications for development of a crustal-scale granitoid pluton and crustal growth. *Geochemistry, Geophysics, Geosystems* **18**, 3340–3358.

Tang, H. F., Su, Y. P., Liu, C. Q., Hou, G. S. & Wang, Y. B. (2007). Zircon U–Pb age of the plagiogranite in Kalamaili belet, Northern Xinjiang and its tectonic implications. *Geotectonica et Metallogenia* **31**, 110–117.

Turner, S. P., Foden, J. D. & Morrison, R. S. (1992). Derivation of some A-type magmas by fractionation of basaltic magma: an example from the Padthaway Ridge, South Australia. *Lithos* **28**, 151–179.

Valley, J. W. (2003). Oxygen isotopes in zircon. In: Hanchar, J. M.Hoskin, P. W. O. (eds) *Zircon*: *Reviews in Mineralogy and Geochemistry*, Mineralogical Society of America and Geochemical Society, 53, Washington, DC, pp. 343–385.

Valley, J. W., Kinny, P. D., Schulze, D. J. & Spicuzza, M. J. (1998). Zircon megacrysts from kimberlite: oxygen isotope variability among mantle melts. *Contributions to Mineralogy and Petrology* **133**, 1–11.

Valley, J. W., Lackey, J. S., Cavosie, A. J., Clechenko, C. C., Spicuzza, M. J., Basei, M. A. S., Bindeman, I. N., Ferreira, V. P., Sial, A. N., King, E. M., Peck, W. H., Sinha, A. K. & Wei, C. S. (2005). 4.4 billion years of crustal maturation: oxygen isotope ratios of magmatic zircon. *Contributions to Mineralogy and Petrology* **150**, 561–580.

Vilalva, F. C. J., Vlach, S. R. F. & Simonetti, A. (2016). Chemical and O-isotope compositions of amphiboles and clinopyroxenes from A-type granites of the Papanduva Pluton, South Brazil: insights into late- to post-magmatic evolution of peralkaline systems. *Chemical Geology* **420**, 186–199.

Watson, E. B. (1979). Zircon saturation in felsic liquids: experimental results and applications to trace element geochemistry. *Contributions to Mineralogy and Petrology* **70**, 407–419.

Wei, C. S., Zhao, Z. F. & Spicuzza, M. J. (2008). Zircon oxygen isotopic constraint on the sources of late Mesozoic A-type granites in eastern China. *Chemical Geology* **250**, 1–15.

White, D. J., Musacchio, G., Helmstaedt, H. H., Harrap, R. M., Thurston, P. C., van der Velden, A. & Hall, K. (2003). Images of a lower-crustal oceanic slab: direct evidence for tectonic accretion in the Archean western Superior province. *Geology* **31**, 997–1000.

Windley, B. F., Alexeiev, D., Xiao, W., Kroner, A. & Badarch, G. (2007). Tectonic models for accretion of the Central Asian Orogenic Belt. *Journal of the Geological Society* **164**, 31–47.

Wu, F. Y., Yang, Y. H., Xie, L. W., Yang, J. H. & Xu, P. (2006). Hf isotopic compositions of the standard zircons and baddeleyites used in U–Pb geochronology. *Chemical Geology* **234**, 105–126.

Xiao, W. J., Windley, B. F., Hao, J. & Zhai, M. G. (2003). Accretion leading to collision and the Permian Solonker suture, Inner Mongolia, China: termination of the central Asian orogenic belt. *Tectonics* **22**, 1069.

Xiao, W., Windley, B. F., Sun, S., Li, J., Huang, B., Han, C., Yuan, C., Sun, M. & Chen, H. (2015). A tale of amalgamation of three permo-triassic collage systems in central Asia: oroclines, sutures, and terminal accretion. *Annual Review of Earth and Planetary Sciences* **43**, 477–507.

Xiao, W. J., Windley, B. F., Yuan, C., Sun, M., Han, C. M., Lin, S. F., Chen, H. L., Yan, Q. R., Liu, D. Y., Qin, K. Z., Li, J. L. & Sun, S. (2009). Paleozoic multiple subduction-accretion processes of the southern Altaids. *American Journal of Science* **309**, 221–270.

Yamaoka, K., Ishikawa, T., Matsubaya, O., Ishiyama, D., Nagaishi, K., Hiroyasu, Y., Chiba, H. & Kawahata, H. (2012). Boron and oxygen isotope systematics for a complete section of oceanic crustal rocks in the Oman ophiolite. *Geochimica et Cosmochimica Acta* **84**, 543–559.

Yang, G., Li, Y., Santosh, M., Yang, B., Zhang, B. & Tong, L. (2013). Geochronology and geochemistry of basalts from the Karamay ophiolitic mélange in West Junggar (NW China): implications for Devonian–Carboniferous intra-oceanic accretionary tectonics of the southern Altaids. *Geological Society of America Bulletin* **125**, 401–419.

Yang, J. H., Wu, F. Y., Chung, S. L., Wilde, S. A. & Chu, M. F. (2006). A hybrid origin for the Qianshan A-type granite, northeast China: geochemical and Sr–Nd-Hf isotopic evidence. *Lithos* **89**, 89–106.

Ye, X. T., Zhang, C. L., Zou, H. B., Yao, C. Y. & Dong, Y. G. (2017). Age and geochemistry of the Zhaheba ophiolite complex in eastern Junggar of the Central Asian Orogenic Belt (CAOB): implications for the accretion process of the Junggar terrane. *Geological Magazine* **154**, 419–440.

Yin, J., Chen, W., Xiao, W., Yuan, C., Windley, B. F., Yu, S. & Cai, K. (2017). Late Silurian–early Devonian adakitic granodiorite, A-type and I-type granites in NW Junggar, NW China: partial melting of mafic lower crust and implications for slab roll--back. *Gondwana Research* **43**, 55–73.

Zeng, L., Niu, H., Bao, Z., Shan, Q., Li, H., Li, N. & Yang, W. (2015). Petrogenesis and tectonic significance of the plagiogranites in the Zhaheba ophiolite, Eastern Junggar orogen, Xinjiang, China. *Journal of Asian Earth Sciences* **113**, 137–150.

Zhang, L., Ren, Z.-Y., Xia, X.-P., Yang, Q., Hong, L.-B. & Wu, D. (2019). In situ determination of trace elements in melt inclusions using laser ablation inductively coupled plasma sector field mass spectrometry. *Rapid Communications in Mass Spectrometry* **33**, 361–370.

Zhang, Z., Yang, L., Teng, J. & Badal, J. (2011). An overview of the earth crust under China. *Earth-Science Reviews* **104**, 143–166.

Zhang, Z., Zhou, G., Kusky, T. M., Yan, S., Chen, B. & Zhao, L. (2009). Late Paleozoic volcanic record of the Eastern Junggar terrane, Xinjiang, Northwestern China: major and trace element characteristics, Sr–Nd isotopic systematics and implications for tectonic evolution. *Gondwana Research* **16**, 201–215.

Zheng, J. P., Sun, M., Zhao, G. C., Robinson, P. T. & Wang, F. Z. (2007). Elemental and Sr–Nd–Pb isotopic geochemistry of Late Paleozoic volcanic rocks beneath the Junggar basin, NW China: implications for the formation and evolution of the basin basement. *Journal of Asian Earth Sciences* **29**, 778–794.

Zhu, Y., Chen, B. O. & Qiu, T. (2015). Geology and geochemistry of the Baijiantan–Baikouquan ophiolitic mélanges: implications for geological evolution of west Junggar, Xinjiang, NW China. *Geological Magazine* **152**, 41–69.

Zhu, Y.-S., Yang, J.-H., Sun, J.-F. & Wang, H. (2017). Zircon HF–O isotope evidence for recycled oceanic and continental crust in the sources of alkaline rocks. *Geology* **45**, 407–410.